NASA TECHNICAL NOTE

NASA TN D-7799

NASA TN D-7799

PERFORMANCE OF A HYPERSONIC HOT FUSELAGE STRUCTURE WITH A CARBON DIOXIDE FROST PROTECTED, NONINTEGRAL CRYOGENIC TANK

Ellsworth L. Sharpe and L. Robert Jackson

Langley Research Center
Hampton, Va. 23665

NATIONAL AERONAUTICS AND SPACE ADMINISTRATION • WASHINGTON, D. C. • MARCH 1975

1. Report No.	2. Government Accession No.	3. Recipient's Catalog No.
NASA TN D-7799		

4. Title and Subtitle	5. Report Date
PERFORMANCE OF A HYPERSONIC HOT FUSELAGE STRUCTURE WITH A CARBON DIOXIDE FROST PROTECTED, NONINTEGRAL CRYOGENIC TANK	March 1975
	6. Performing Organization Code
7. Author(s)	8. Performing Organization Report No.
Ellsworth L. Sharpe and L. Robert Jackson	L-9711
	10. Work Unit No.
9. Performing Organization Name and Address	501-22-06-01
NASA Langley Research Center Hampton, Va. 23665	11. Contract or Grant No.
	13. Type of Report and Period Covered
12. Sponsoring Agency Name and Address	Technical Note
National Aeronautics and Space Administration Washington, D.C. 20546	14. Sponsoring Agency Code

15. Supplementary Notes

16. Abstract

A model which consisted of a hot structure and a nonintegral tank protected by a carbon dioxide frost thermal protection system was tested under the following conditions: (1) room temperature loading and (2) heating and loading corresponding to the Mach 8 flight of an air-breathing launch vehicle. In the simulated flight tests, liquid nitrogen inside the tank was withdrawn at the rate fuel would be consumed. Prior to each simulated flight test, carbon dioxide was cryodeposited in the insulation surrounding the tank; during the tests, subliming CO_2 frost absorbed heat and provided a purge gas for the space between the tank and the structure. A method of flame spraying the joints between panels with a nickel-aluminum material was developed to prevent excessive leakage of the purge gas through the outer structure. The tests indicated that the hot structure (with a joint repaired by riveting), the nonintegral tank and suspension system, and the carbon dioxide frost thermal protection system provide a workable concept with predictable performance.

17. Key Words (Suggested by Author(s))	18. Distribution Statement
Carbon dioxide frost Thermal protection system Gas purge system Cryogenic tankage Hot structures Hypersonic structures	Unclassified – Unlimited STAR Category 33

19. Security Classif. (of this report)	20. Security Classif. (of this page)	21. No. of Pages	22. Price*
Unclassified	Unclassified	48	$3.75

*For sale by the National Technical Information Service, Springfield, Virginia 22151

PERFORMANCE OF A HYPERSONIC HOT FUSELAGE STRUCTURE WITH A CARBON DIOXIDE FROST PROTECTED, NONINTEGRAL CRYOGENIC TANK

By Ellsworth L. Sharpe and L. Robert Jackson
Langley Research Center

SUMMARY

To study fuselage tankage for hypersonic vehicles, a model representing a section of fuselage of a Mach 8 air-breathing launch vehicle was designed, fabricated, and tested. The model consists of a hot structure of René 41 alloy with Z-stiffened skin surrounding a nonintegral cryogenic tank of aluminum alloy with a carbon dioxide frost thermal protection system. The model was loaded at room temperature, and strain-gage data were recorded. The model was subjected to tests in which the flight of a hypersonic launch vehicle was simulated by heating and loading while liquid nitrogen inside the tank was withdrawn at the rate fuel would be consumed. Prior to each simulated flight test, carbon dioxide was cryodeposited in the insulation bonded to the tank.

Both the model and test apparatus were modified as the investigation progressed. The modifications included: increasing the strength of spotwelded joints between panels of the outer skin by adding rivets, reducing purge gas leakage through the outer skin by flame spraying panel joints with a nickel-aluminum material, and adding a gas circulation and heating system which mixed the purge gases and maintained an ambient outer skin temperature during preflight simulation.

The results of the experiments were compared with results obtained analytically for both structural and thermal responses. The results of the study indicated that with the above modifications the hot structure, the nonintegral tank and suspension system, and the carbon dioxide frost thermal protection system performed as predicted by the thermal and structural analysis.

INTRODUCTION

Studies of hypersonic airplanes have been predicated on the use of liquid hydrogen as a fuel (refs. 1 and 2). Liquid hydrogen is of interest for such applications because of its high heat of combustion and its high cooling capacity. However, its low density – 73.1 kg/m^3 (4.56 lbm/ft^3) – leads to large tankage volumes, and the manner in which this cryogenic fuel is contained can strongly influence configuration weights.

With uncooled structures, large temperature gradients exist between the structure and the tank, which can cause thermal stress problems. At the high heat fluxes associated with hypersonic flight in the atmosphere, large portions of the vehicle surface structure will reach temperatures above 1144 K (1600° F); whereas, the temperature of hydrogen tanks will be 21 K (-423° F), a temperature difference of over 1111 K (2000° F). Thus, tank suspension systems are required that permit unrestrained thermal expansion, but support tank inertial loads. The large temperature difference also imposes critical insulation requirements to avoid excessive fuel boiloff.

The low temperature of liquid hydrogen presents another problem in that air reaching the tank surface will condense and thereby create a partial vacuum which pumps in more air, a process called cryopumping. Meanwhile, the condensate flows down the tank wall, drips from the insulation onto the hot structure and evaporates, and then recondenses on the tank wall. This continuous pumping action transfers large quantities of heat from the hot structure to the tank and produces wasteful boiloff of the liquid hydrogen (refs. 3 and 4).

Finally, the small molecular size of hydrogen and its consequent propensity to leak, together with the large range of fuel-air ratios for combustion, and the low energy required for ignition make it desirable to create an inert space between the tank and structure.

One solution to these problems which is successfully used for land-based storage is to enclose the tank in a vacuum. Unfortunately, flight-weight sealed systems (refs. 5 and 6) have proven to be unreliable, and they are considered to be beyond the present state of the art. For example, in reference 7, attempts to fabricate an evacuated flight-weight structure were terminated when, after repeated trials, a leak-free structure could not be obtained.

Another approach, which has been used in some spacecraft, is to purge the space between the tank and structure with helium. Helium is the only gas that does not liquefy at liquid hydrogen temperatures, and thus, does not cryopump. Helium-purged thermal protection systems have been the subject of two extensive studies. (See refs. 5 and 8.) The simplicity of the system is a decided asset; however, helium is a rare and costly gas and its high thermal conductivity makes helium-purged systems inefficient (heavy) (ref. 8).

A third approach, investigated in this study, makes use of carbon dioxide frost, which is cryodeposited within a layer of fibrous insulation prior to each flight. (See refs. 6, 9, and 10.) At pressures below 5 atm, carbon dioxide has no liquid phase and thus cannot establish the continuous pumping action exhibited by other condensable gases. Furthermore, carbon dioxide can be deposited as a low density, low conductivity frost (ref. 10). During flight, aerodynamic heating causes the frost to sublime. The sublimation process not only supplies a purge gas of low conductivity to the system, but also absorbs heat that would otherwise be transferred to the hydrogen fuel.

In this study, a conical model representing a hypersonic vehicle fuselage with an outer structure of René 41 alloy and a nonintegral aluminum alloy tank protected by a carbon dioxide frost thermal protection system was subjected to thermal and structural loads typical of those to be encountered in the flight of a Mach 8 air-breathing launch vehicle. During the investigation the model, test apparatus, and experimental procedures were modified to improve the performance. Results of the tests are presented and compared with analytical performance predictions.

SYMBOLS

Values are given in both SI and U.S. Customary Units. The measurements and calculations were made in U.S. Customary Units.

d	insulation thickness
E	modulus of elasticity
K_f	fixity factor
L	unsupported length
M	total bending moment
N_ϕ	meridional force per unit width
$N_{\phi\theta}$	shear force per unit width
P_m	force exerted by moment jack
P_s	force exerted by shear jack
r	radius
T	temperature
t	metal thickness
$\bar{t}$	effective skin thickness (includes contribution of stiffeners)

V	transverse shear load applied to model
x	frost thickness
α	coefficient of thermal expansion
β	percent of carbon dioxide (partial pressure) in the purge gas mixture during frost deposition
ϵ	strain
ϵ_n	strain at gage location n
ϵ_x, ϵ_y	strain at principal axis
θ	angular coordinate (see fig. 9)
μ	Poisson's ratio
σ_{cr}	critical stress
σ_{th}	thermal stress
τ	time
Ω	cone half-angle
ω	mass of frost deposited per unit tankage area

DESIGN CONSIDERATIONS

The fuselage model, shown in figure 1, which was designed to simulate part of the first stage of a two-stage, hypersonic vehicle, utilized the carbon dioxide frost, hot-skin stringer-structure concept of reference 6. This concept was selected in lieu of other more efficient concepts investigated in the same reference because it was believed to be more nearly at the state of the art and, although somewhat heavier, would provide an acceptable mass fraction for the intended application. The full-scale vehicle would have a maximum diameter of approximately 6.1 m (20 ft) and fuel tanks up to 12.2 m (40 ft) in length.

The trajectory for the vehicle included an ascent flight period of 11 minutes to Mach 8, a 2g pull-up for launching an orbiter stage, and an equilibrium glide period of about 21 minutes. The pull-up at Mach 8 provided the limit load condition combining maximum air loads and maximum material temperature. Thermal and structural analysis of the fuselage at these flight conditions indicated that surface temperatures up to 1078 K (1480^{o} F) and compressive stress resultants in the range from 87.6 to 525.4 kN/m (500 to 3000 lb/in.) would be encountered. For these low structural indices the least weight design is buckling controlled, provided the yield strength is sufficiently high to insure elastic behavior. René 41 was selected for the primary structure because of its high modulus and yield strength at the design temperature.

Outer skins, Z-stiffeners, and ring frames for the primary structure were sized by minimum weight proportions in an axial compression analysis in which equal local buckling, panel buckling, and general instability strength were used, along with a maximum ratio of radius of gyration to effective thickness for the panel cross section. For the compressive load of 222.4 kN/m (1270 lb/in.), selected for the point design, the analysis yielded a structure with a unit mass of 13.0 kg/m^2 (2.67 lbm/ft^2). Wall construction of the model was identical to the full-scale design; therefore, because of the reduced diameter, the model was not critical in general instability.

The optimization procedure yielded shallower and more closely spaced Z-stiffeners than are generally encountered in conventional construction; moreover, since welding was selected for attaching the skin to the stiffeners, a new approach to skin-stringer fabrication was employed. Instead of attaching each stringer to the frames and then attaching the skin to the stringers, a preassembled panel approach was used, as shown in figure 2. Panels from one to three frame spacings long, consisting of a skin section, end doublers, and Z-stiffeners, were resistance spotwelded together as a subassembly. These panels were resistance spotwelded to the ring frames, and a closure skin was heli-arc spotwelded over the joint. Thus, the entire assembly could be accomplished from outside the fuselage.

The nonintegral tank was of 2219 aluminum alloy waffle construction. Aluminum alloys were selected primarily because of their superior resistance to hydrogen embrittlement, and the 2219 alloy was selected because of its weldability and fracture toughness. The tank was designed for an internal pressure of 345 kPa (50 psig). The waffle pattern was optimized for a full-scale compressive edge load of 175 kN/m (1000 lb/in.) by considering both local and general buckling. The use of this optimization method resulted in a tank unit mass of 11.0 kg/m^2 (2.25 lbm/ft^2).

The tank suspension system must permit differential thermal expansion between the tank and the primary structure while simultaneously maintaining support for the tank inertial loads. In addition, heat transfer to the tank through the supports must be low. With

a hot structure at 1144 K (1600° F) and a 12.2-m-long (40 ft) tank, the longitudinal differential expansion may be as much as 25 cm (10 in.). The tank suspension system for this study (see figs. 1 and 3) consisted of thrust fittings at the tank midlength and concentric bellows supports at each end of the tank. Midlength thrust fittings halve the expansion to be accommodated at each end of the tank. Bellows supports provide little restraint against axial or rotational movement, but are stiff against transverse movement. (Differential axial movement across the diameter of the bellows permits rotational movement.) Thus, the bellows offer simple end support for all loads acting normal to the longitudinal center line of the tank. Furthermore, they tend to distribute the loading on the periphery of the tank and structure.

A corrugated skirt is attached between the bellows and tank wall to permit differential radial expansion. (Expansion is accommodated by fanlike spreading of the hot end of the corrugation and by flexing of small flats provided in the skirt at the ends of the corrugations, as shown in fig. 3.) To provide the flexibility and the thermal isolation desired, both the bellows and the skirt were fabricated of thin gage, relatively low conductivity Inconel 718, and insulated on both sides.

As indicated in reference 9, the CO_2 frost thermal protection system offered the least weight of the known purge systems. For the present application, the thermal protection system was designed to limit the tank temperature to 311 K (100° F) or less. Analysis indicated that the lower tank surface, which was in contact with the fuel during ascent flight, maintained a peak temperature of less than 311 K (100° F) when the thermal protection system was optimized, based on fuel boiloff, but the upper tank surface was overheated. Therefore, the upper surface became the governing factor and was used to size the thickness of the thermal protection system. As indicated in reference 6, the average total mass of insulation, CO_2 frost, and fuel boiloff is only 5.37 kg/m^2 (1.10 lbm/ft^2).

MODEL DESCRIPTION

Structure and Tank

The model, shown in the sketch of figure 1 and in the photographs of figure 4, is 1.38 m (54.5 in.) long with end diameters of approximately 0.41 m and 0.91 m (16.3 in. and 36.0 in.) and a half-cone angle of 10.24°. The conical shape and the model size were selected so that the model could be tested in the Langley 8-foot high-temperature structures tunnel.

The primary structure, which consists of Z-stiffened skin panels stabilized by Y-section and box section ring frames, is fabricated from solution-treated René 41 alloy. The ring frames are built-up sheet metal assemblies joined by spotwelding. Machined

end rings are provided for attaching the model to the test apparatus. Structural panels consist of a 0.046-cm-thick (0.018 in.) outer skin, 0.038-cm-thick (0.015 in.) Z-stiffeners, and 0.046-cm-thick (0.018 in.) doublers at the fore and aft ends of each panel. In each panel, the Z-stiffener pitch varies longitudinally, because the stiffeners are attached to the skin on the straight-line elements of the conical surface. Each upper and lower panel has a nominal Z-pitch of 1.94 cm (0.75 in.) at the larger end of the panel. Side panels have a nominal Z-pitch of 3.8 cm (1.5 in.) at the larger end. The preassembled panels are welded to the stabilizing rings from outside the model. More details on the assembly procedure for the Z-stiffened panel structure are given in reference 11.

The tank was constructed from 2219 aluminum alloy waffle plate by fusion welding several preformed sections together in the shape of a truncated cone. The sections included the following: a one-piece formed front bulkhead, eight conical side panel segments, a T-section ring frame welded midway inside the conical tank, an aft bulkhead weldment, and a bolt flange for attaching an access door. The access door is a one-piece formed bulkhead with an attachment flange welded to it. Fill and vent lines, consisting of formed tubes and machined flanges joined by fusion welding, are bolted to matching bosses welded to the access door. Teflon seals are used at all bolted joints to prevent leakage.

At each end of the tank, corrugated skirts of Inconel 718 are riveted to short aluminum sleeves welded to the outside of the tank. Bellows are bolted to the corrugated skirts and to the end ring frames of the structure. These bellows, which support the tank, are formed from 0.102-cm-thick (0.040 in.) annealed Inconel 718 sheet, reduced in thickness at the convolutions by chemical milling to permit the required longitudinal deflection at low force. (See ref. 11.)

Machined male thrust fittings are located on the top and on the bottom of the tank forward of the Y-frame. Matching female thrust fittings of sheet metal are welded to the primary structure. The tank is installed through the large end of the model; then the mating thrust fittings are engaged by rotating the tank several degrees to provide fore-and-aft thrust connections. Finally, the bellows are bolted in place at both ends. The design allows the access door to be removed from the large end of the model without removing the tank from the structure.

Insulation blankets are bonded to the outside surface of the tank and clipped to both sides of the corrugated skirts. The insulation blankets, which consist of layers of quartz-fiber insulation encapsulated by quartz cloth, were machine stitched with Teflon-coated quartz thread. The joints in insulation blankets are coincident with the joints in the tank wall to permit inspection of the tank welds without removal of the insulation. The average thickness of the insulation was 0.90 cm (0.35 in.).

Carbon Dioxide Frost Thermal Protection System

The carbon dioxide frost thermal protection system, illustrated in the wall section drawing of figure 1(b), consists of fibrous insulation against the cryogenic tank into which carbon dioxide frost is cryodeposited from a two gas mixture prior to each simulated flight test. During flight, aerodynamic heating (simulated by radiant heating in the laboratory) causes the carbon dioxide frost to sublime. Gas resulting from this sublimation purges the space around the tank during flight. In addition, heat that would otherwise transfer to the fuel and result in wasteful boiloff is absorbed as the frost sublimes and transpires through the insulation. Thus, the carbon dioxide frost thermal protection system not only prevents cryopumping of air to the cold wall, but also absorbs some of the heat that would produce fuel boiloff.

The efficiency of this system depends on the density of the frost deposited (refs. 6 and 9). In reference 10, details of the process used to deposit carbon dioxide frost are outlined. In the present study, insulation blankets identical to those on the model were tested in the cryodeposition chamber of reference 10 to determine the parameters required for depositing the necessary thickness and density of frost. Results of these deposition tests are described in appendix A.

LABORATORY APPARATUS

For safety purposes, experiments were conducted in an enclosure with remote controls provided for all the test apparatus. The apparatus was electrically isolated from the enclosure because of the high voltage supplied to the heaters.

Support Stand and Hydraulic Load System

The support stand, shown schematically in figure 5, supports the model and provides a rigid frame from which loads are applied. The model is cantilevered horizontally from a cylindrical plenum attached to the vertical leg of the stand. This plenum is open to the aft end of the model to allow introduction of purge gases into the space between the tank and the structure. A door is provided at the rear of the plenum chamber to enable access to the inside of the model. Instrumentation and plumbing required for the model enter the plenum space through ports on the plenum chamber adjacent to the door.

Forward of the model, two hydraulic jacks are mounted to the base leg of the stand. The jack nearer the model applies an upward force to the model. The other jack applies a bending moment to the model through a bell crank attached to the base leg of the stand by a pivot-slip joint. The pivot-slip joint allows the bell crank not only to rotate about the joint axis but also to slide parallel to the model to permit unrestrained model expansion when heated. Turnbuckles, which connect the bell crank to the load fixture, allow

the crank portion of the pivot-slip joint to be positioned properly relative to the slot in the support stand.

Heaters are installed on the plenum chamber and on the loading fixture flanges to which the model is fastened so that thermal mismatch between the model and test apparatus can be minimized during the heating tests.

Radiant Heaters and Temperature Control System

Banks of quartz-lamp radiant heaters were used to heat the model. As shown in figure 6, these heaters were supported by two stands that separated about the vertical center plane of the model to enable access to the model between experiments. Figure 6(a) shows the heater stand open; figure 6(b) shows it closed, as would be the case during a test. Each of the heaters consisted of a water-cooled, gold-plated copper reflector, grooved for contact cooling 16 quartz lamps, each 0.953 cm (0.375 in.) in diameter and 25.4 cm (10 in.) long. The heaters were divided into zones to allow independent control of temperatures at the bottom, sides, and top of the model to simulate aerodynamic heating at an angle of attack. Power to the three zones was supplied by a three-phase ignitron power supply which could be preprogramed to impose the desired temperature histories on the hot skin.

Cryogenic Storage and Transfer System

Liquid nitrogen, used as the cryogenic fluid throughout this test program, was supplied by the cryogenic storage and transfer system shown schematically in figure 7. Four 200-liter liquid nitrogen Dewars were connected so that two were connected in series with each other but in parallel with the other two. Two Dewars could be pressurized to fill the model while the other two were being refilled from outside the enclosure. The plumbing for the Dewars allowed them to be filled either from outside the enclosure or from the model when the model was being emptied. The plumbing also allowed the Dewars to be vented while being filled from either direction or to be pressurized to supply cryogenics to the model.

The transfer line from the Dewars to the model was insulated. Pneumatic valves were located in both the cryogenic supply and vent lines going into and out of the model. With the model vent line closed and the supply line open, the tank could be pressurized with nitrogen gas to empty the tank into the vented Dewars. All valves associated with the Dewars, shown in figure 7, had electrically insulated Teflon stems and could be hand operated from outside the enclosure.

Pressure relief valves and rupture disks were provided at each Dewar, at the tank, and between any two valves to insure that pressure buildups resulting from trapped cryogenics would not cause hazardous failures. Pressure gages measuring the pressure in the tank and in the Dewars were located at the control panel.

Purge Gas System

The purge gas system, shown schematically in figure 8, could supply nitrogen, helium, carbon dioxide, and various mixtures of these gases to the model. Each of these gases was supplied from standard gas cylinders through a manifold equipped with a pressure regulator. (The carbon dioxide was heated by an electric heater before passing through the pressure regulator to prevent freezing of the expanding gas.) The pressure-regulated gases were fed through control valves located in the control panel into a common manifold. From there, the gases flowed through a thermostatically controlled heater into the plenum which supplied the model. The composition of purge gas mixture was monitored with a partial pressure measuring system. A circulating fan and a heater were added in the course of the investigation to improve the uniformity of the CO_2-He mixture and to avoid condensation and freezing of water vapor on the outside surface of the model during the frost deposition phase of the operation.

Instrumentation and Data Acquisition

The instrumentation and data acquisition equipment included the following: pressure gages, a gas analyzer, pressure transducers, flowmeters, thermocouples, strain gages, and both remote high-speed and onsite printout recorders. Details of the use of several of these items appear in the following paragraphs.

A partial pressure measuring instrument (gas analyzer), accurate to 0.1 percent, was used to monitor the ratio of CO_2 partial pressure to the mixture pressure in the purge space during frost cryodeposition. Details of this instrument can be found in reference 12. Samples of purge gas were drawn from six stations in the purge space around the tank in the model through tubes. Sample stations were located at $\theta = 90^{\circ}$ and 270° near the front and rear of the model, respectively, and at 0°, 90°, 180°, and 270° at the midpoint of the model. The tubes were valved and connected so that a partial pressure ratio at individual stations or an average partial pressure ratio at all the stations could be read.

Strain gages were located at the upper and lower surfaces and at the side surfaces, as illustrated in the schematic drawing of figure 9. (Note that the gages on the side are at 90° to one another and 45° to the horizontal.) The upper and lower surface gages were used to determine longitudinal inplane stresses and the side surface gages were used to determine shear stresses. In addition, gages were applied to the Z-stiffeners, as indicated in figure 9.

Chromel-alumel thermocouples were welded to the structure in 20 places and positioned in the tank insulation in 30 places. Copper-constantan thermocouples were welded to the outer surface of the tank in 10 places and placed inside the tank at three elevations to indicate liquid level. Figure 10 shows the locations of: liquid level thermocouples which were used to determine the rate at which LN_2 was removed from the tank, outer

skin thermocouples which were used to control the hot surface temperatures, and tank thermocouples for which data are presented in the report.

EXPERIMENTS AND PROCEDURES

Room Temperature Load-Strain Tests

Three separate room temperature tests were run to relate the stresses in the structure to the applied bending moment and shear load. In the first test, bending moment alone was applied; in the second test, shear load alone was applied; and in the third test, both bending and shear loads were applied. During all three tests, the loads were applied in five equal increments. The maximum shear load (P_s) was 21.35 kN (4800 lb) and the maximum load on the moment jack (P_m) was 64.19 kN (14 430 lb), which represents a moment of 32.61 kN-m (288 600 in-lb). The same values were used for combined loads. These loads were greater than those subsequently used for the simulated flight test to account for the higher material properties at room temperature. At each loading increment, outputs of the strain gages and of pressure transducers placed in the hydraulic lines to measure loads were recorded.

Simulated Hypersonic Flight Tests

The model was subjected to three complete thermal cycles of simulated flight and one partial cycle. During the first and third complete thermal cycles, mechanical loads were also applied.

The complete cycle of simulated hypersonic flight for the third test is shown in figure 11 and included a pretest (preflight) phase and a test (flight) phase. In the pretest phase, the tank was filled with cryogen, carbon dioxide frost was deposited in the fibrous insulation, and the tank was pressurized. In the test phase, heating was applied, the tank was emptied, loads were applied and released, and the tank pressure was relieved. Although the procedure differed slightly among the three tests as techniques were improved, the tests were generally performed as follows: Initially, the plenum chamber and purge space were purged and lightly pressurized (less than 6.9 kPa (1 psi) above ambient) with CO_2. Once all the air was purged from the system, as indicated by the partial-pressure measuring instrument, helium gas was added. The flow of the two gases (He and CO_2) was adjusted to obtain the required mixture to deposit the necessary frost thickness and density. The cryogenic tank was then filled as rapidly as possible with liquid nitrogen. As cryodeposition began, the purge gas flows were readjusted to maintain the required mixture. (During the last test, the circulating fan and thermostatically controlled heater were used to maintain the uniformity of the mixture and to provide a constant purge gas supply temperature of 297 K (75° F).) After the required quantity of CO_2 frost was deposited, as determined from elapsed time and prior deposition tests, the

deposition process was halted by purging the system with nitrogen. (Initially, a helium purge was used, but it was found that the cheaper nitrogen purge gas was satisfactory when the cryogenic fluid was also nitrogen.) Pressurization of the purge system was maintained with nitrogen gas until it was replaced in the simulated flight cycle by the subliming CO_2 as the purge gas.

The test (flight) phase simulated the heating, fuel consumption, and limit load of the launch vehicle, as shown in figure 11. Powered flight for this vehicle terminated at the end of 11 min in a staging maneuver in which maximum aerodynamic heating and loading occurred. For the tests, heat was supplied by quartz-lamp radiant heaters programed to provide the same heating cycle presented in reference 6. During the initial portion of the heating cycle, the liquid nitrogen was emptied from the model tank to simulate the time of fuel consumption, as shown in figure 11. Mechanical loads were slowly applied to the model through the loading fixture, and reached a maximum when the temperature peaked. The loads were held at their maximum values $\left(P_s = 13.34 \text{ kN } (3000 \text{ lb}) \text{ and } P_m = 35.59 \text{ kN } (8000 \text{ lb}) \text{ (18.08 kN-m (160 000 in-lb) total moment)}\right)$ for approximately 2 minutes to insure loading at the time of peak temperature, and then slowly released.

Model Leak Tests

Difficulty was experienced in purging the model of air and in maintaining a positive pressure in the purge space during the initial simulated flight test. To investigate this problem, the model was removed from the test stand and the leakage rate of the structure was measured. For these measurements, closeout plates were bolted to each end of the model. A pressure gage and a tube attached to the purge gas supply were connected to one of these plates. Purge gas, either CO_2 or helium, was supplied to the model and flow rates (read from a flowmeter in the gas supply line) were recorded as a function of purge-space pressure.

RESULTS AND DISCUSSION

Primary Structure

Room temperature load tests.- Strains measured during the room temperature tests for shear, bending moment, and shear plus bending-moment loadings are presented in table I. These results are compared with analytical results in figure 12.

The analytical results were based on equations for stress resultants in a conical shell derived for the loading conditions of this study. The derivation used membrane theory similar to that of reference 13. The following equations were used:

$$N_\phi = \frac{M \cos \theta}{\pi r^2 \cos \Omega} \tag{1}$$

$$N_{\phi\theta} = \left(\frac{M \tan \Omega}{\pi r^2} - \frac{V}{\pi r}\right) \sin \theta \tag{2}$$

where M and V are total bending moment and transverse shear load, respectively, at the cross section of interest. These equations were applied at the forward strain-gage station (see fig. 9), and the results were converted to strain by the equations

$$\epsilon = \frac{N_\phi}{E\bar{t}} \tag{3}$$

$$\epsilon_x - \epsilon_y = \frac{2N_{\phi\theta}(1 + \mu)}{Et} \tag{4}$$

The analytical and experimental values of strain at the top ($\theta = 0^o$) and bottom ($\theta = 180^o$) of the model at the forward strain-gage station (ϵ_1 and ϵ_2) are plotted in figure 12(a) as a function of the local moment. It can be seen that the experimental data for all three loading conditions obtained as the model was loaded (unflagged symbols) agree well with the straight-line theoretical variation predicted by equations (1) and (3), the agreement being slightly better in tension than in compression. Comparison of the loading data with unloading data indicates considerable hysteresis (as indicated by a comparison of flagged and unflagged symbols). The hysteresis is apparently due to friction in the loading system. Apart from the hysteresis, a slight nonlinearity is noted during loading in the compression data (unflagged symbols at the highest loading). This nonlinearity may be due to the proximity of the strain-gage station to the end of the model or to initial imperfections in the model. However, at the maximum load, the measured strain represents a stress of 179 MPa (26 000 psi), which is near the proportional limit of the solution-treated René 41 (186 MPa (27 000 psi)), and some local yielding may have occurred.

The analytical and experimental values of the shear strain ($\epsilon_7 - \epsilon_8$) at the side of the model ($\theta = 90^o$) for the same forward station are presented as functions of the local moment in figure 12(b). The agreement between experiment and theory is good when the model is loaded by the shear jack only, but is poor when it is loaded with the bending-moment jack. An examination of the strain-gage readings for gages 7 and 8 in tables I(b) and I(c) shows that the strains are opposite in sign but not equal in magnitude as would be the case if there was pure shear strain at the horizontal center plane as expected. A strain-gage rosette would be required to attain the correct shear strain, but the reason for departure from pure shear strain remains unexplained.

The lack of any significant departure of the experimental data from a linear strain-load relationship indicated that buckling did not occur up to the maximum load imposed, which was the room temperature equivalent of the design limit load.

Simulated flight tests.- After the model was subjected to the heating of the initial simulated flight, it was found that the closure skin had buckled locally at the circumferential joints between panels. These circumferential buckles can be observed in figure 13(a). It was also discovered that only a marginal clearance existed in the pivot-slip joint of the loading mechanism; consequently, the possibility existed that the model could have been overloaded because of a failure of the mechanism to accommodate thermal expansion. The joints were repaired by spotwelding and the model was again exposed to the temperature cycle of a simulated flight. This time the mechanical loads were not applied, and care was taken to assure that there was adequate clearance in the pivot joint to allow for model thermal expansion; nevertheless, as can be seen in figure 13(b), local buckling reoccurred at the joints. (The light color bands along the joints in fig. 13(b) are flame sprayed material used to seal the joints as will be discussed in a subsequent section.)

After this second failure, the design of the joints between panels, shown in figure 14, was examined in more detail. For strength purposes, it was desired to have the closure skin 0.091 cm thick (0.036 in.). However, to improve the weldability (see ref. 11), the thickness of the closure skin over the flanges was reduced to 0.046 cm (0.018 in.) by chemical milling. As a consequence of the chemical milling and the difference in pitch of the Z-stiffeners of the two panels, only in the areas indicated by the hatching in figure 14 was the original thickness of the closure retained. Although placed as close to the ends of the Z's as practical, the fusion spotwelds joining the closure skin to the Z's were about 0.48 cm (0.1875 in.) from the end; thus a narrow unsupported strip ($L \approx 0.95$ cm (0.38 in.)) in which the buckles occurred is formed. From the failures it was apparent that the heli-arc spotwelds failed to hold the closure skin in contact with the ends of the Z-stiffeners; however, it was not apparent whether the buckles or the spotweld failures occurred first.

The model was repaired again; however, this time, instead of welding the closure skin to the Z-stiffeners, rivets were used and were inserted as close to the end of each Z as possible to reduce the unsupported length of the joint. (The center line of the rivets was approximately 0.64 cm (0.25 in.) from the ends of the Z's; however, the 0.64-cm-diameter (0.25 in.) heads of the rivets reduced the unsupported length of the closure skin.) The repaired model was first subjected to an abbreviated thermal cycle (up to maximum temperature without mechanical loading) and then to a complete simulated flight cycle with both heating and loading (test 3). There was no sign of buckling after either test.

Despite the successful test, a stress and buckling analysis of the joint area (details given in appendix B) indicates that the joint was at least marginal, if not inadequate. The analysis indicates that thermal stress, resulting from the temperature difference through the panel thickness (hot skin to Z inner flange), is sufficient to produce local

buckling of a 0.046-cm (0.018 in.) closure strip with an unsupported length L of 0.95 cm (0.375 in.). A conceptual design intended to overcome both the performance and fabrication problems encountered with the present closure is shown in figure 15. The design features a thickened closure skin (0.091 cm (0.036 in.)) and avoids the welding difficulties by substituting rivets for the spotwelds.

Unlike many designs for thin-sheet construction, the present model was designed for the hot skin to be fully load bearing (that is, no local buckling or rippling between stiffeners). Examination of the model after the simulated flight tests (see fig. 13) indicated that no inelastic buckling occurred.

Tank and tank suspension.- The tank and seals successfully withstood the low temperature of 75 K (-325° F) and a pressure of 345 kPa (50 psig) without leakage. In addition to the simulated flight test, the tank was filled and pressurized over 10 times and the access door was removed several times during the preliminary checkout of the test setup; thus, a reuse capability of the tank and seals was indicated.

The elements of the tank support system appear to have performed their respective functions without difficulty with the exception of the forward bellows which experienced some cracking. The problem with the forward bellows was apparently associated with the small diameter of the bellows and would not be encountered with a full-scale vehicle. As stated in reference 11, the forward bellows had to be thinned considerably to provide the desired axial flexibility. In the chemical milling process, the forward bellows were actually milled through in one spot. During tests, the forward bellows developed cracks in the highly thinned convolutions. It is significant to note, however, that the larger diameter rear bellows, which provided the required flexibility with a greater metal thickness, did not crack.

Circumferential extension of the corrugations in the tank skirts during the simulated hypersonic flight tests appears to have alleviated thermal stresses. Moreover, the thermal isolation of the tank from the hot structure, afforded by the insulated skirt, also was effective, since the test results of the thermal protection system indicated no significant extraneous heat transferred to the tank walls. Tank wall temperatures agreed with predicted temperatures for a one-dimensional heat transfer through the model wall. The tests indicate that a corrugated skirt of the type used in the model is suited to tank suspension.

CO_2 Frost Thermal Protection System

Thermal performance.- Temperature histories for the model during the simulated flight tests are presented in figure 16. As discussed in appendix A, a carbon dioxide frost density of 801 kg/m^3 (50 lbm/ft^3) was used for the first two tests, and a density of 561 kg/m^3 (35 lbm/ft^3) was used for the third. Figure 16(a) contains the results for

the first test (previously reported in ref. 14) and figure 16(b) contains results for the third test. (Results for the second test were omitted because they were essentially identical to the first test results.) The two upper curves in both figures are the preprogramed surface temperatures that were applied to the structure. The input temperature profile for the first test (fig. 16(a)) was based on an equilibrium glide at a constant angle of attack during descent, which produced an oscillatory flight path and consequently, oscillatory aerodynamic heating. These oscillations were smoothed for the third test (fig. 16(b)) on the assumption that, in an actual flight, a pilot would modulate the angle of attack to prevent these large excursions. In addition to the variation in input temperature, the time required for the cryogenic tank to empty differed from the planned 11 minutes. For the first test about 20 minutes were required; whereas, for the third test 13 minutes were required.

The ablation option of the analysis method of reference 15 was used to predict the temperatures for the top and bottom of the cryogenic tank, shown by the curves at the bottom of the two figures. In using the analysis to determine tank temperature histories, the frost system was treated as a charring ablator, the CO_2 frost-insulation composite acting as the uncharred material, and the insulation outside the frost acting as a nonreceding char layer. In addition, the following assumptions were made: (1) At the start of the heating cycle (takeoff), no liquid was in contact with the upper tank surface; (2) at the start of the heating cycle, liquid was in contact with the lower tank surface and remained in contact until the tank was empty (20 min for test 1 and 13 min for test 3); (3) the frost layer was evenly deposited around the tank and had a density of either 801 kg/m^3 (50 lbm/ft^3) (test 1) or 561 kg/m^3 (35 lbm/ft^3) (test 3); and (4) the thermal properties of the carbon dioxide frost were those presented in reference 9.

Two significant temperature plateaus can be observed for the lower surface in the tank temperature histories shown in figure 16. When liquid is present, the temperature rises as heat is applied until it reaches the boiling temperature of the liquid nitrogen in the pressurized tank. (When the tank was pressurized at the beginning of the test, the boiling temperature of the liquid nitrogen was increased; thus, the liquid nitrogen that was initially saturated at atmospheric pressure became subcooled.) Once all the liquid has been heated to the higher boiling temperature, no further increase in temperature is possible until the liquid is withdrawn; therefore, the first temperature plateau is the boiling temperature of the pressurized liquid nitrogen. A second plateau is reached when the tank temperature reaches the carbon dioxide frost sublimation temperature, and the tank temperature remains at the sublimation temperature until all frost has sublimed from the insulation at the location observed. The upper surface is at the sublimation plateau for a considerable portion of the test period.

Comparison of experiment (symbols) and analysis (curves) in figure 16 indicates that (1) the thermophysical property data used in the analysis were adequate, (2) the cryodeposition data used in the experiment were reliable, and (3) the performance of the carbon dioxide frost thermal protection system can be predicted. Moreover, examination of the insulation blankets and their attachment to the tank revealed no damage from the freezing and outgassing of the carbon dioxide or from the temperatures experienced during the simulated hypersonic flight tests.

Structural sealing.- Difficulties in attaining and in maintaining a positive pressure in the purge space were experienced in the first simulated flight test because of excessive leakage at the butt joints between panels, despite the fact that there was a spotwelded doubler behind each joint. To alleviate this problem, a technique for sealing these joints was developed. A nickel-aluminum (96-percent Ni, 4-percent Al) material was flame sprayed on the joints, burnished with a hand grinder (to reduce porosity), and resprayed with additional material. Photographs of the model in figure 13 show the model before and after flame spraying.

Prior to the flame spraying of the model, small samples of the flame-sprayed joints were tested to demonstrate the thermal compatibility of the René 41 structural skin and the flame spray material. A joint made of two sheets of René 41 butted together, with a doubler spotwelded to each sheet (similar to the joints in the model), was flame sprayed using the techniques described above. The joint was sawed into strips (coupons) that were between 1.27 cm (0.5 in.) and 2.54 cm (1 in.) wide. Ten coupons, each having a portion of the joint (saw cuts were perpendicular to the joint), were cycled in an oven with an air environment. A cycle consisted of heating the coupons to 1200 K (1700° F), holding the temperature constant for 1/2 hr, and then allowing the coupons to cool down to room temperature. After 50 cycles the coupons were visually unchanged, and the flame spray material and the René 41 appeared to be compatible.

Results of leakage tests of the model before and after flame spraying are illustrated in the plots of pressure against flow rate of figure 17. The data indicate the amount of purge gas per unit surface area required to maintain a given pressure in the model. The two curves are helium and carbon dioxide leakage rates for the model after the joints were flame sprayed. The two points located high above the curves on the graph represent the data obtained before flame spraying. (One point is for helium and the other is for carbon dioxide.) Comparing flow at the same pressure indicates that leakage was reduced 84 percent for helium and 70 percent for carbon dioxide by the nickel-aluminum flame spray.

Purge gas circulation and heating.- During the frost deposition phase of the initial tests, it was found that the purge gas concentration varied by as much as 10 percent at different stations within the purge space, and water vapor would condense and freeze on

the outer surface of the model. To alleviate these problems, a thermostatically controlled, heated circulation system for the purge gas (see fig. 8), which did not allow the temperature of the circulating purge gas to go below 297 K (75° F), was installed. The heating and circulating of the purge gas mixture not only thoroughly mixed the purge gas (the variation in CO_2 concentration was within 1 percent over the purge space) but also maintained the external surface temperature of the model above the dewpoint, and thus prevented condensation. In view of the importance of purge gas concentration on frost cryodeposition (ref. 10), and because a vehicle may sit for a long period with liquid hydrogen onboard, similar circulation and heating systems will probably be necessary during ground hold for hydrogen-fueled vehicles.

CONCLUSIONS

In this study, a model representing a section of the fuselage of a Mach 8 launch vehicle was subjected to heating and loading representative of a typical hypersonic flight trajectory. The model consisted of a nickel alloy, flight weight, hot structure containing a nonintegral cryogenic tank of aluminum alloy. The tank was protected by a carbon dioxide frost thermal protection system.

The model and the test apparatus were modified as required to improve their performance. These modifications included fastening the outer skins and doublers between panels to the Z-stiffeners with rivets to prevent local buckling of the closure skin between panels, flame spraying all joints in the outer skin with a nickel-aluminum material to limit the leakage of the purge gas from the model, and installing a circulation system which heated and mixed the purge gas (consisting of helium and carbon dioxide) during frost cryodeposition prior to a simulated flight test.

From a comparison of the experimental results with the analytical predictions, it can be concluded:

1. The hot structure with the modified (riveted) joints between panels, the nonintegral tank, and the tank suspension system sustained the simulated flight environment; however, analysis indicates that the joint design is marginal.

2. The carbon dioxide frost thermal protection system performs as predicted and offers the potential of light, reusable protection for liquid hydrogen tanks.

3. Leakage of purge gas through structural joints was significantly reduced by flame spraying a nickel-aluminum material on the joints between panels.

4. The circulation and the heating of the purge gases during simulated ground hold prevented water condensation on the outer skin of the model and maintained a uniform mixture of purge gases.

Langley Research Center,
National Aeronautics and Space Administration,
Hampton, Va., December 4, 1974.

APPENDIX A

CARBON DIOXIDE FROST DEPOSITION

Since there is no way of knowing by direct measurement the frost thickness and density that are present in the model, the parameters controlling the deposition process must be determined and controlled. Based on the results of some of the preliminary deposition tests of reference 10, attempts were made to establish a frost density of 401 kg/m^3 (25 lbm/ft^3) for the first two simulated flight tests. (This frost density was recommended in ref. 9 as a compromise between minimum weight and adequate strength.) Subsequently, however, as the investigation of reference 10 progressed and a better understanding of the factors affecting frost deposition was developed, it was determined that the actual frost density for tests 1 and 2 was about 801 kg/m^3 (50 lbm/ft^3).

By the time of the third simulated flight test, deposition tests had been conducted by using the cryodeposition chamber of reference 10 with the cryogenic tank covered with insulation blankets identical to those for the fuselage model. For these tests, the purge gas pressure and outer tank temperature were maintained at 6.9 kPa above ambient (1 psig) and 300 K (80° F), respectively. Results of the tests are presented as carpet plots in figure 18, and in figure 19 as functions of the parameters that were found to correlate the data as single curves for mass and frost thickness as presented in reference 10. (In both figs. 18 and 19, point A is the data used in simulated flight tests 1 and 2, whereas, point B represents the deposition parameters of test 3.)

From the data of figure 18, it is apparent that at a frost density of 401 kg/m^3 (25 lbm/ft^3) the maximum amount of frost that could be deposited in the 0.9-cm-thick (0.35 in.) insulation was 2.44 kg/m^2 (0.5 lbm/ft^2). (The design thickness of the blankets was 1.27 cm (0.5 in.); however, they became compacted during fabrication.) By using the thermal analysis method of reference 15, it was found that with this amount and density of frost, the tank temperature at the end of the simulated flight trajectory would approach the maximum allowable temperature for an aluminum tank. Consequently, to provide a larger temperature margin, the higher density frost (point B) was selected for the third test.

APPENDIX B

BUCKLING OF THE CLOSURE SKIN BETWEEN PANELS

During the initial simulated flight test, a temperature difference of over 278 K (500° F) was recorded between the outer skin and the inner flange of the Z-stiffeners. Thermal stress in the panels σ_{th} due to this temperature difference can be approximated by

$$\sigma_{th} = E\alpha\,\Delta T \tag{B1}$$

where

E modulus of elasticity

α coefficient of thermal expansion

$\Delta T = T_1 - T_{av}$

T_1 temperature at outer surface

T_{av} area-weighted average temperature of panel cross section

The bending moment M resulting from the thermal stress can be determined by substituting the solution of equation (B1) into the following equation:

$$M = \frac{\sigma_{th} I}{c} \tag{B2}$$

where I and c are the panel moment of inertia and the centroidal distance to the outer skin, respectively. This moment must be transmitted across the joint between panels by the closure skin acting in conjunction with the outer flange of the supporting ring. The resulting joint stress in the closure skin σ_j is given by the following equation:

$$\sigma_j = \frac{Mc_j}{I_j} \tag{B3}$$

where I_j and c_j are the joint moment of inertia and the centroidal distance to the other skin, respectively. The solution to equation (B3) yields 437 MPa (63 350 psi).

An approximation of the stresses σ_{cr} required to buckle a thin, narrow strip, such as the closure skin, is obtained from Euler's equation

$$\delta_{cr} = \frac{K_f \pi^2 E t^2}{12(1 - \mu^2)L^2} \tag{B4}$$

where

K_f fixity factor

t metal thickness

μ Poisson's ratio

L unsupported length (axial distance between end welds)

The fixity factor, which depends on the end support, is difficult to determine. (For simply supported edges, $K_f = 1$; for clamped edges, $K_f = 4$.) By assuming that $K_f = 1.0$, $L = 0.953$ cm (0.375 in.), and $t = 0.0457$ cm (0.018 in.) (this assumption does not include any added strength which is obtained from the 0.0914-cm (0.036 in.) portion of the closure skin), equation (B4) yields a critical buckling stress σ_{cr} equal to 395 MPa (57 265 psi) and indicates that the closure skin would buckle from thermal stress.

REFERENCES

1. Knip, Gerald, Jr.; and Allen, John L.: Analysis of Booster Systems with a Recoverable Hypersonic Airplane First Stage. AIAA Paper No. 64-543, May 1964.

2. Osmun, Willian G.: Hypersonic Propulsion. Space/Aeronaut., vol. 41. no. 3, Mar. 1964, pp. 80-83.

3. Scott, Russell Burton: Cryogenic Engineering. D. Van Nostrand Co., 1959.

4. McGrew, J. L.: A Comparative Study of Airborne Liquid-Hydrogen Tank Insulation. Advances in Cryogenic Engineering, Volume 8, K. D. Timmerhaus, ed., Plenum Press, Inc., 1963, pp. 387-392.

5. Heathman, John H.; and Kelley, Larry G.: Hydrogen Tankage for Hypersonic Cruise Vehicles. AIAA/ASME Seventh Structures and Materials Conference, Apr. 1966, pp. 430-438.

6. Jackson, L. Robert; Davis, John G., Jr.; and Wichorek, Gregory R.: Structural Concepts for Hydrogen-Fueled Hypersonic Airplanes. NASA TN D-3162, 1966.

7. Hirsch, Richard P.: Development of Techniques and Fabrication of a Structural Model for Research on Structures for Hypersonic Aircraft. NASA CR-66211, [1966].

8. Norton, Allan M.: Advanced Structural Concepts Experimental Program – Project ASCEP. Volume II – Experimental Evaluations. AFFDL-TR-67-146, Vol. II, U.S. Air Force, June 1968. (Available from DDC as AD 838 134.)

9. Jackson, L. R.; and Anderson, M. S.: A Carbon Dioxide Purge and Thermal Protection System for Liquid Hydrogen Tanks of Hypersonic Airplanes. Advances in Cryogenic Engineering. Volume 12, Plenum Press, Inc., 1967, pp. 146-156.

10. Sharpe, Ellsworth L.: The Control of Carbon Dioxide Cryodeposits. NASA TN D-7334, 1973.

11. Hopkins, John C.: Fabrication Process Developments of a Structural Model for Research on Hydrogen-Fueled Hypersonic Vehicles. NASA CR-66198, 1967.

12. Melfi, Leonard T., Jr.; and Wood, George M., Jr.: The Use of an Ionization Gage as a Quantitative Analyzer for Bi-Gaseous Mixtures. NASA TN D-1597, 1962.

13. Timoshenko, Si; and Woinowsky-Krieger, S.: Theory of Plates and Shells. Second ed., McGraw-Hill Book Co., Inc., 1959.

14. Jackson, L. Robert; and Sharpe, Ellsworth L.: A Carbon Dioxide Purge and Thermal Protection System for Liquid Hydrogen Tanks. Conference on Hypersonic Aircraft Technology, NASA SP-148, 1967, pp. 501-513.

15. Swann, Robert T.; Pittman, Claud M.; and Smith, James C.: One-Dimensional Numerical Analysis of the Transient Response of Thermal Protection Systems. NASA TN D-2976, 1965.

TABLE I.- STRAIN-GAGE READINGS

(a) Bending-moment load only

Strain gage	Strain-gage readings at percent maximum bending load of –										
	0	22	42	63	83	100	83	63	42	21	0
1	0.001×10^{-3}	-0.092×10^{-3}	-0.189×10^{-3}	-0.287×10^{-3}	-0.388×10^{-3}	-0.472×10^{-3}	-0.426×10^{-3}	-0.338×10^{-3}	-0.236×10^{-3}	-0.118×10^{-3}	-0.010×10^{-3}
2	.000	-.125	-.258	-.398	-.544	-.669	-.606	-.484	-.339	-.178	-.004
3	.000	.110	.235	.368	.501	.610	.555	.448	.317	.174	.017
4	.000	.105	.226	.354	.484	.591	.539	.433	.306	.166	.016
5	-.001	-.077	-.146	-.223	-.301	-.367	-.319	-.237	-.161	-.086	-.010
6	.000	.072	.126	.197	.270	.330	.278	.191	.113	.050	-.009
7	.001	-.120	-.230	-.333	-.437	-.522	-.456	-.342	-.238	-.126	-.017
8	.000	.137	.269	.388	.510	.607	.531	.403	.281	.145	.005
9	.000	-.098	-.209	-.319	-.433	-.533	-.488	-.400	-.296	-.171	-.029
10	.001	-.056	-.119	-.192	-.268	-.330	-.301	-.242	-.170	-.095	-.019
11	.000	-.036	-.086	-.139	-.191	-.231	-.219	-.187	-.134	-.069	.004
12	.000	-.030	-.071	-.112	-.157	-.189	-.176	-.151	-.107	-.057	.002
13	-.001	.012	.033	.053	.074	.090	.083	.068	.046	.021	-.008
14	-.001	.039	.095	.157	.219	.271	.257	.221	.159	.087	.003
15	.000	-.035	.068	-.100	-.133	-.162	-.139	.105	-.074	-.040	.002
16	.001	.020	.033	.052	.073	.088	.072	.047	.024	.011	.000
19	.000	-.015	-.037	-.058	-.080	-.099	-.094	-.082	-.062	-.035	-.003
20	.001	-.006	-.018	-.034	-.051	-.065	-.061	-.053	-.037	-.021	.000
21	.000	-.119	-.248	-.385	-.527	-.646	-.588	-.474	-.334	-.178	-.011
22	.000	.113	.240	.372	.503	.609	.555	.448	.316	.169	.010
23	.000	-.106	-.206	-.315	-.424	-.516	-.449	-.336	-.230	-.126	-.015
24	.000	.089	.164	.256	.347	.426	.367	.262	.168	.083	0
28	.000	-.060	-.127	-.202	-.280	-.341	-.313	-.253	-.178	-.099	-.018
29	-.001	-.028	-.070	-.114	-.161	-.199	-.190	-.165	-.121	-.067	.005
30	.000	.029	.071	.115	.162	.200	.192	.168	.124	.072	.009
31	.000	-.021	-.039	-.060	-.081	-.097	-.083	-.058	-.037	-.017	.000
32	.000	.021	.040	.060	.081	.098	.084	.063	.043	.022	-.001
35	.000	-.011	-.025	-.041	-.056	-.067	-.062	-.051	-.037	-.018	-.002
36	.000	-.003	-.010	-.019	-.029	-.037	-.037	-.034	-.024	-.013	-.001

TABLE I.- STRAIN-GAGE READINGS – Continued

(b) Shear load only

Strain gage	Strain-gage readings at percent maximum shear load of –										
	0	24	44	64	84	100	81	60	40	21	0
1	0.000×10^{-3}	-0.018×10^{-3}	-0.044×10^{-3}	-0.067×10^{-3}	-0.091×10^{-3}	-0.109×10^{-3}	-0.107×10^{-3}	-0.080×10^{-3}	-0.054×10^{-3}	-0.027×10^{-3}	-0.001×10^{-3}
2	-.001	-.024	-.057	-.087	-.121	-.146	-.143	-.107	-.073	-.039	-.001
3	.000	.025	.059	.090	.123	.147	.142	.105	.071	.037	.000
4	.000	.023	.054	.086	.117	.141	.138	.103	.069	.038	.002
5	.001	.035	.078	.124	.169	.206	.191	.142	.097	.053	.005
6	0	-.045	-.099	-.157	-.213	-.259	-.241	-.184	-.127	-.074	-.012
7	.000	.052	.113	.171	.230	.276	.257	.191	.128	.070	.006
8	.000	-.053	-.114	-.174	-.232	-.280	-.261	-.195	-.131	-.071	-.006
9	.000	-.018	-.045	-.069	-.097	-.117	-.114	-.088	-.060	-.034	-.003
10	-.001	-.018	-.043	-.067	-.093	-.113	-.110	-.085	-.060	-.033	-.003
11	0	-.043	-.097	-.148	-.199	-.237	-.224	-.166	-.111	-.058	-.001
12	-.001	-.035	-.078	-.119	-.164	-.197	-.185	-.138	-.093	-.050	-.002
13	.000	.015	.036	.057	.076	.093	.086	.063	.042	.019	.004
14	.000	.051	.114	.175	.236	.284	.271	.204	.139	.076	.006
15	.000	.017	.036	.055	.072	.087	.080	.060	.039	.022	.002
16	-.001	-.018	-.039	-.064	-.087	-.107	-.100	-.077	-.054	-.032	-.005
19	0	-.016	-.036	-.055	-.075	-.090	-.086	-.064	-.044	-.024	-.002
20	-.001	-.015	-.037	-.059	-.079	-.096	-.091	-.068	-.047	-.023	-.001
21	.000	-.024	-.059	-.091	-.127	-.153	-.150	-.114	-.079	-.044	-.004
22	0	.027	.063	.098	.135	.163	.159	.120	.082	.045	.004
23	.001	.048	.105	.165	.223	.272	.253	.192	.132	.075	.011
24	.000	-.049	-.110	-.172	-.236	-.288	-.268	-.203	-.141	-.082	-.014
28	.000	-.016	-.038	-.058	-.079	-.096	-.094	-.071	-.048	-.027	-.002
29	0	-.038	-.089	-.136	-.184	-.222	-.211	-.159	-.107	-.059	-.004
30	0	.037	.087	.134	.182	.220	.210	.160	.111	.062	.008
31	.000	.015	.033	.051	.069	.084	.079	.060	.041	.023	.003
32	.000	-.012	-.026	-.040	-.054	-.065	-.061	-.045	-.031	-.017	-.002
35	-.001	-.007	-.018	-.026	-.036	-.043	-.039	-.030	-.020	-.010	-.001
36	.000	-.016	-.035	-.055	-.074	-.090	-.086	-.065	-.045	-.024	-.002

TABLE I.- STRAIN-GAGE READINGS – Concluded

(c) Both shear and moment loads applied

Strain gage	Strain-gage readings at percent maximum bending load and percent maximum shear load, respectively, of –										
	0 0	21 23	42 42	62 61	84 80	100 100	83 78	66 58	42 40	21 21	0 0
1	0	-0.110×10^{-3}	-0.233×10^{-3}	-0.356×10^{-3}	-0.478×10^{-3}	-0.588×10^{-3}	-0.530×10^{-3}	-0.435×10^{-3}	-0.288×10^{-3}	-0.150×10^{-3}	0.000×10^{-3}
2	$.000 \times 10^{-3}$	-.145	-.312	-.483	-.660	-.822	-.745	-.611	-.403	-.214	-.011
3	.000	.133	.288	.442	.598	.734	.662	.540	.349	.181	.002
4	0	.127	.277	.430	.585	.721	.651	.531	.343	.180	.003
5	0	-.037	-.068	-.095	-.129	-.151	-.123	-.105	-.056	-.027	-.001
6	0	-.022	-.030	-.042	-.063	-.067	-.043	-.032	-.005	-.011	-.006
7	0	-.057	-.102	-.137	-.176	-.198	-.164	-.144	-.088	-.040	-.002
8	0	.074	.144	.196	.254	.291	.249	.216	.141	.068	.001
9	0	-.115	-.249	-.379	-.510	-.635	-.578	-.479	-.326	-.178	-.013
10	.000	-.074	-.158	-.249	-.347	-.437	-.398	-.324	-.210	-.114	-.013
11	.000	-.081	-.180	-.274	-.349	-.417	-.378	-.295	-.178	-.067	-.058
12	.000	-.065	-.147	-.225	-.291	-.351	-.317	-.248	-.151	-.060	-.039
13	0	.031	.071	.118	.163	.208	.187	.146	.095	.048	.002
14	.000	.091	.206	.133	.453	.567	.524	.428	.290	.162	.014
15	0	.019	-.037	-.051	-.068	-.082	-.072	-.065	-.048	-.030	-.007
16	.000	-.001	-.008	-.015	-.018	-.028	-.033	-.030	-.031	-.021	-.005
19	.000	-.032	-.073	-.114	-.160	-.201	-.186	-.153	-.106	-.060	-.008
20	0	-.025	-.057	-.095	-.133	-.171	-.158	-.127	-.086	-.048	-.005
21	-.001	-.142	-.306	-.143	-.646	-.807	-.733	-.603	-.400	-.214	-.013
22	0	.137	.298	.459	.620	.760	.690	.565	.370	.195	.005
23	-.001	-.053	-.099	-.139	-.186	-.216	-.180	-.153	-.088	-.043	-.001
24	.000	.034	.057	.081	.115	.129	.098	.081	.029	.008	.003
28	0	-.075	-.159	-.251	-.347	-.434	-.395	-.323	-.209	-.113	-.011
29	0	-.068	-.157	-.250	-.352	-.450	-.419	-.342	-.235	-.136	-.025
31	0	-.006	-.007	-.007	-.010	-.010	-.004	-.005	-.001	-.002	-.001
32	.000	.009	.016	.022	.030	.035	.029	.027	.017	.010	.002
35	0	-.020	-.044	-.068	-.090	-.109	-.100	-.082	-.056	-.029	-.002
36	0	-.019	-.044	-.074	-.104	-.134	-.124	-.100	-.067	-.037	-.003

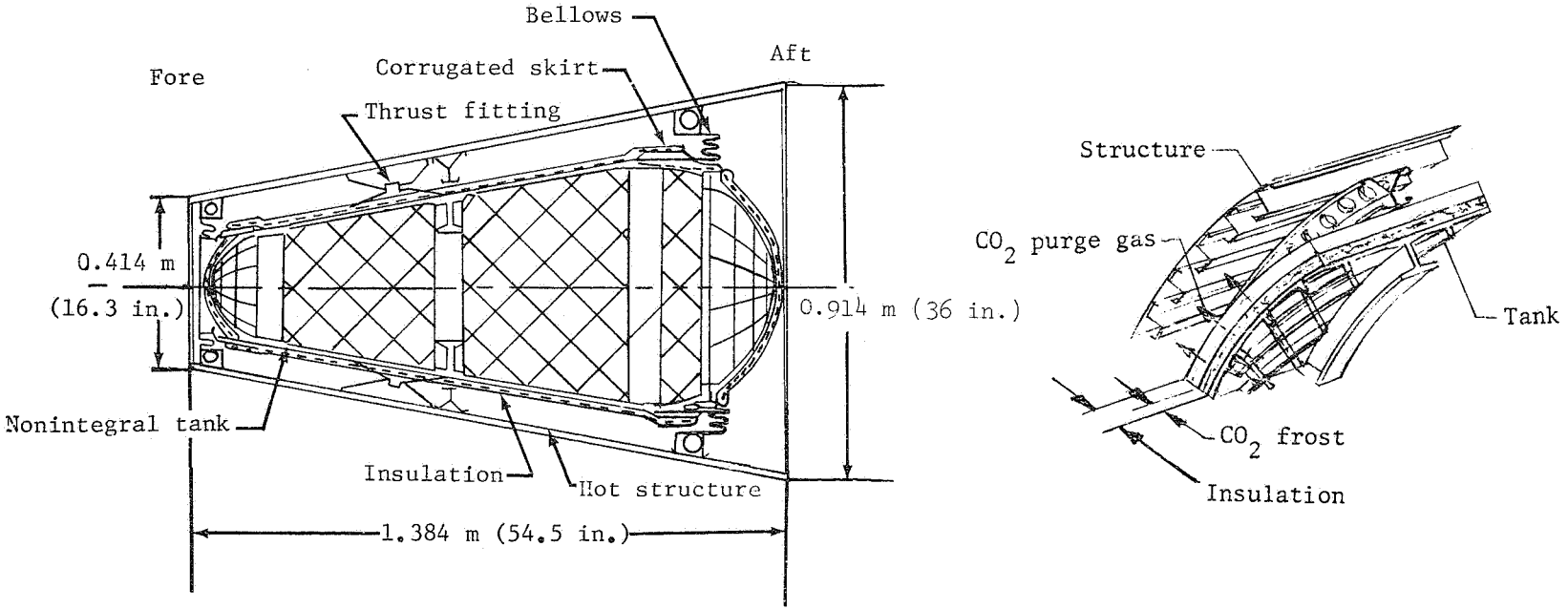

(a) Longitudinal section.

(b) Wall section.

Figure 1.- Hot structural model with nonintegral tank and CO_2 purge system.

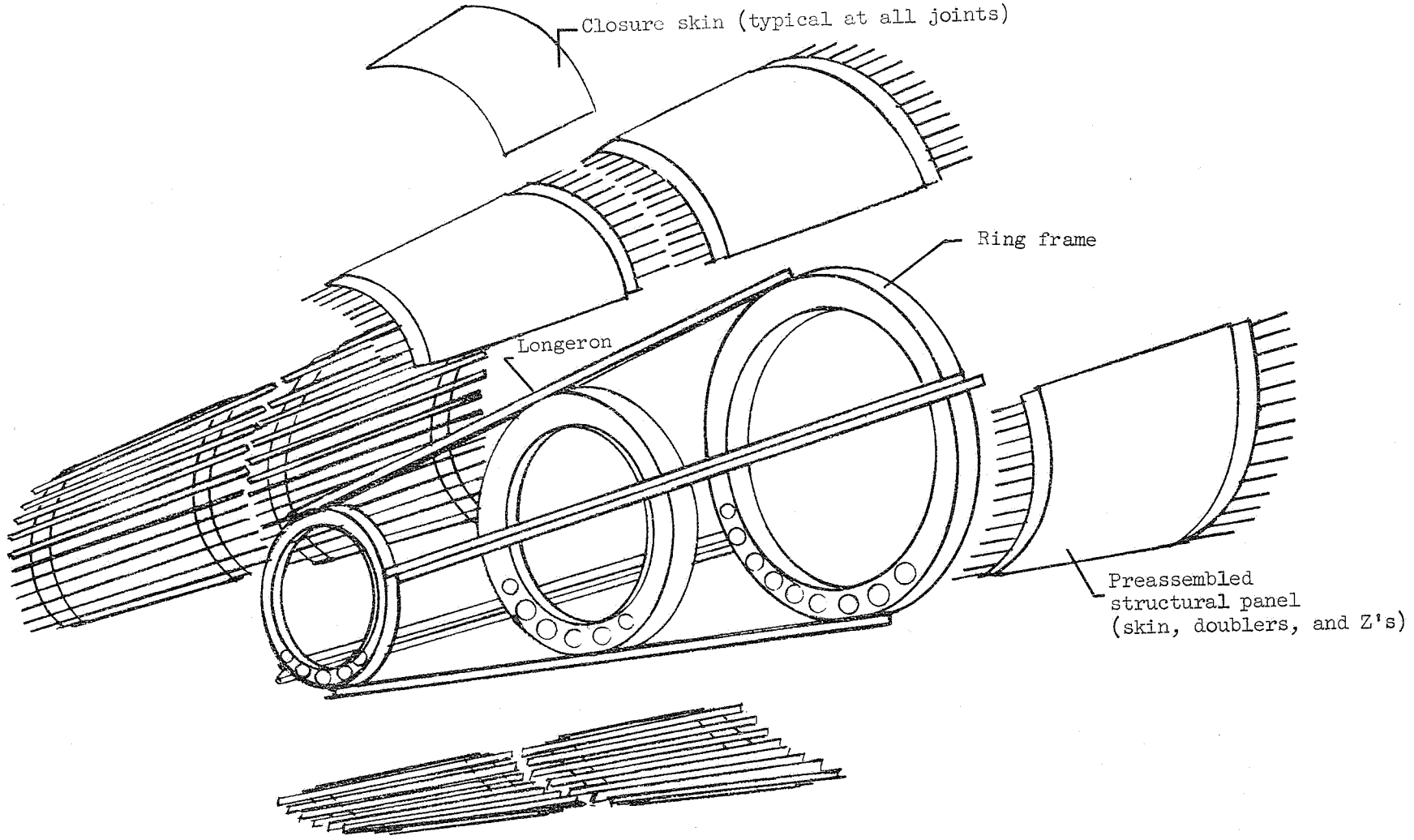

Figure 2.- Fabrication schematic for hot structure with preassembled structural panels.

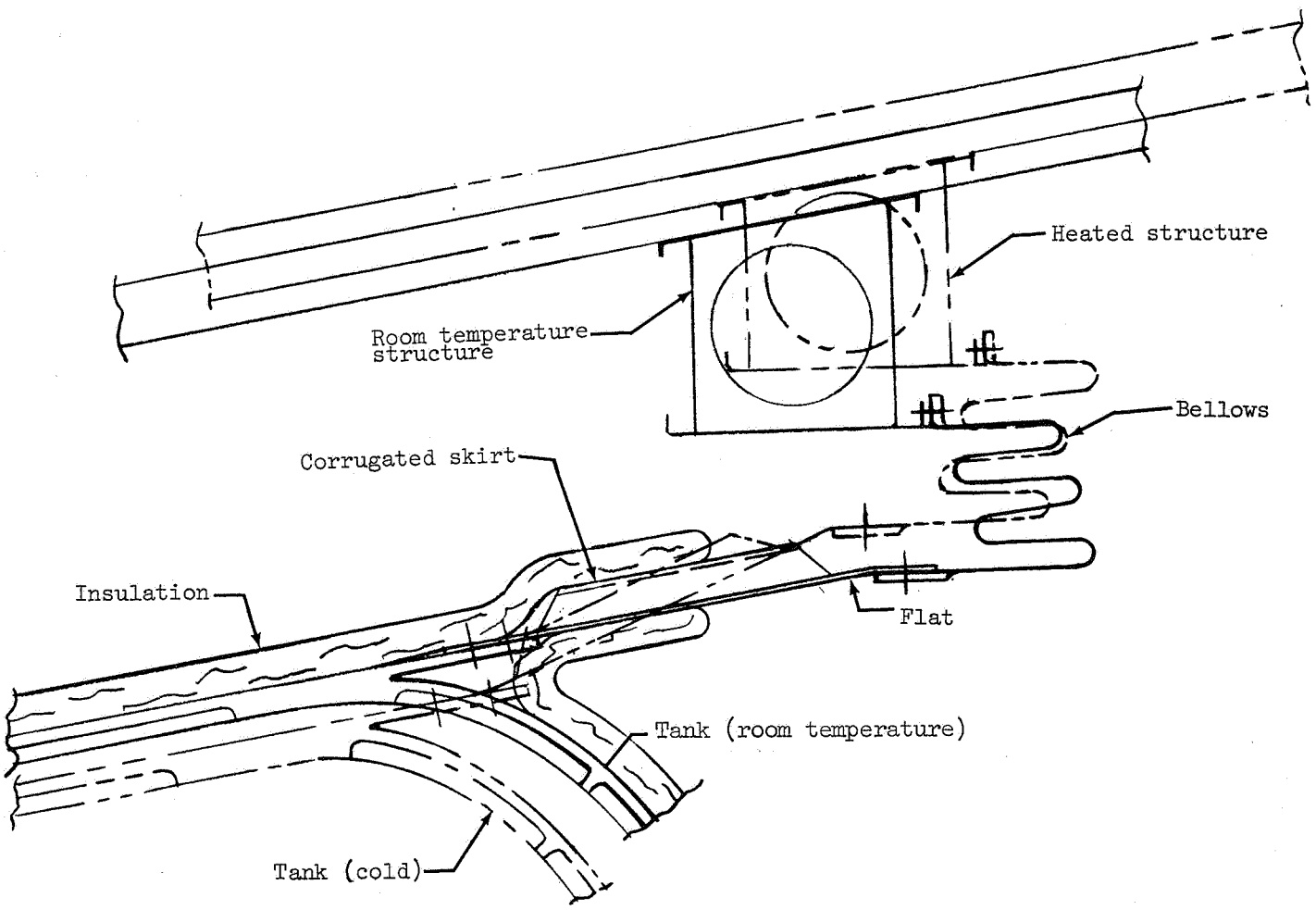

Figure 3.- Tank suspension system.

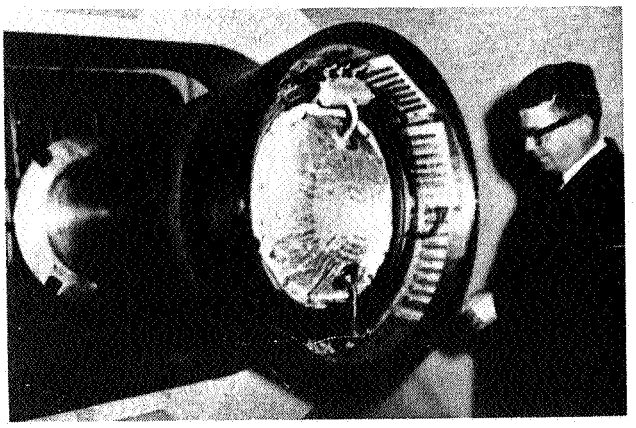

(a) Hot structure with nonintegral tank.

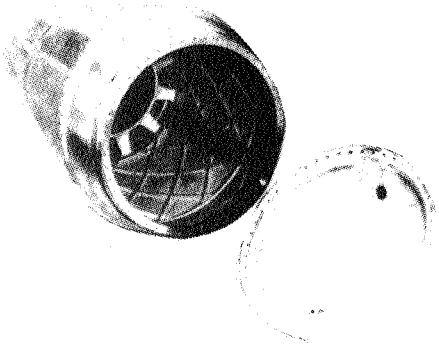

(b) Aluminum tank with access door removed.

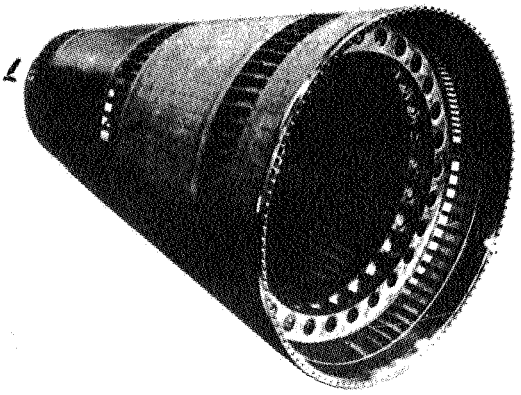

(c) Hot structure without closure skins.

Figure 4.- Hot structural model and components. L-74-8542

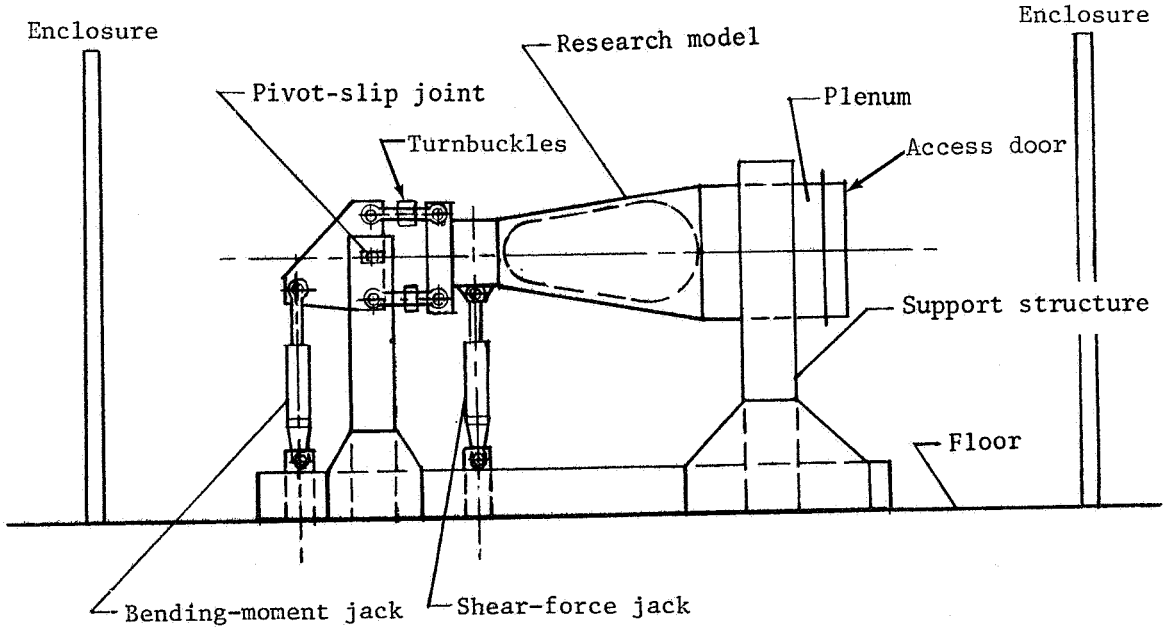

Figure 5.- Hydraulic loading and support system.

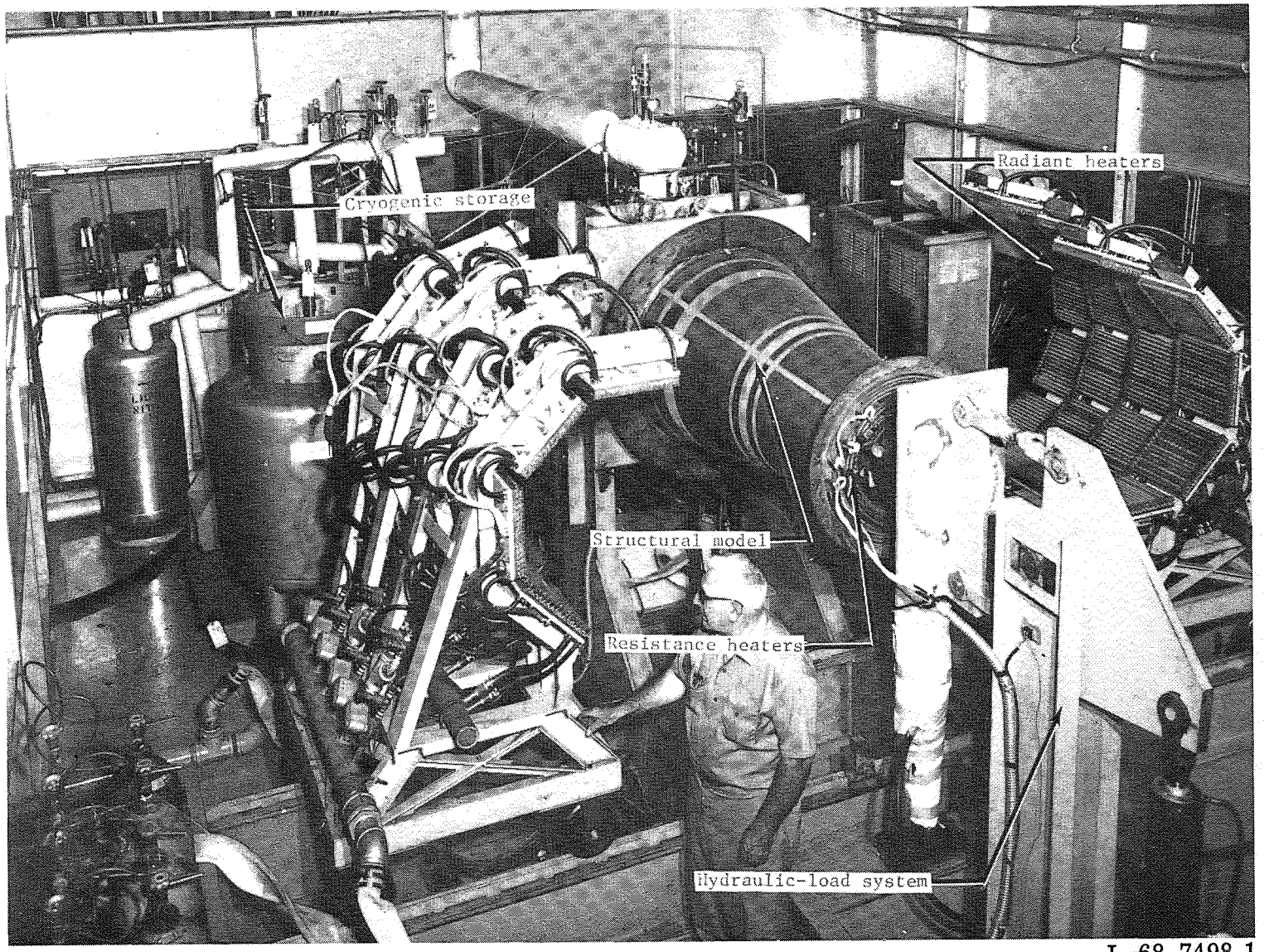

L-68-7498.1

(a) Heater stand open.

Figure 6.- Model and test apparatus.

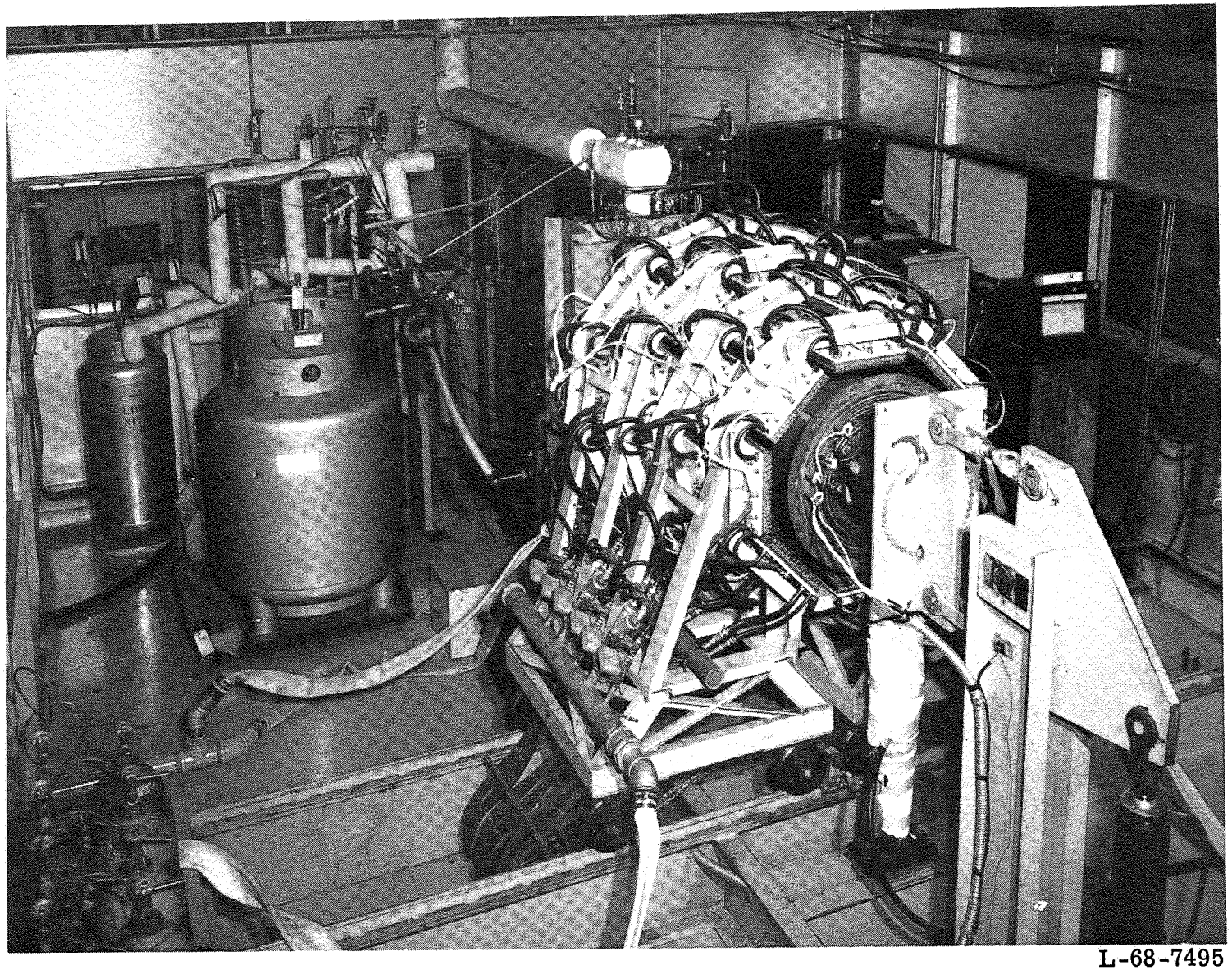

L-68-7495

(b) Heater stand closed.

Figure 6.- Concluded.

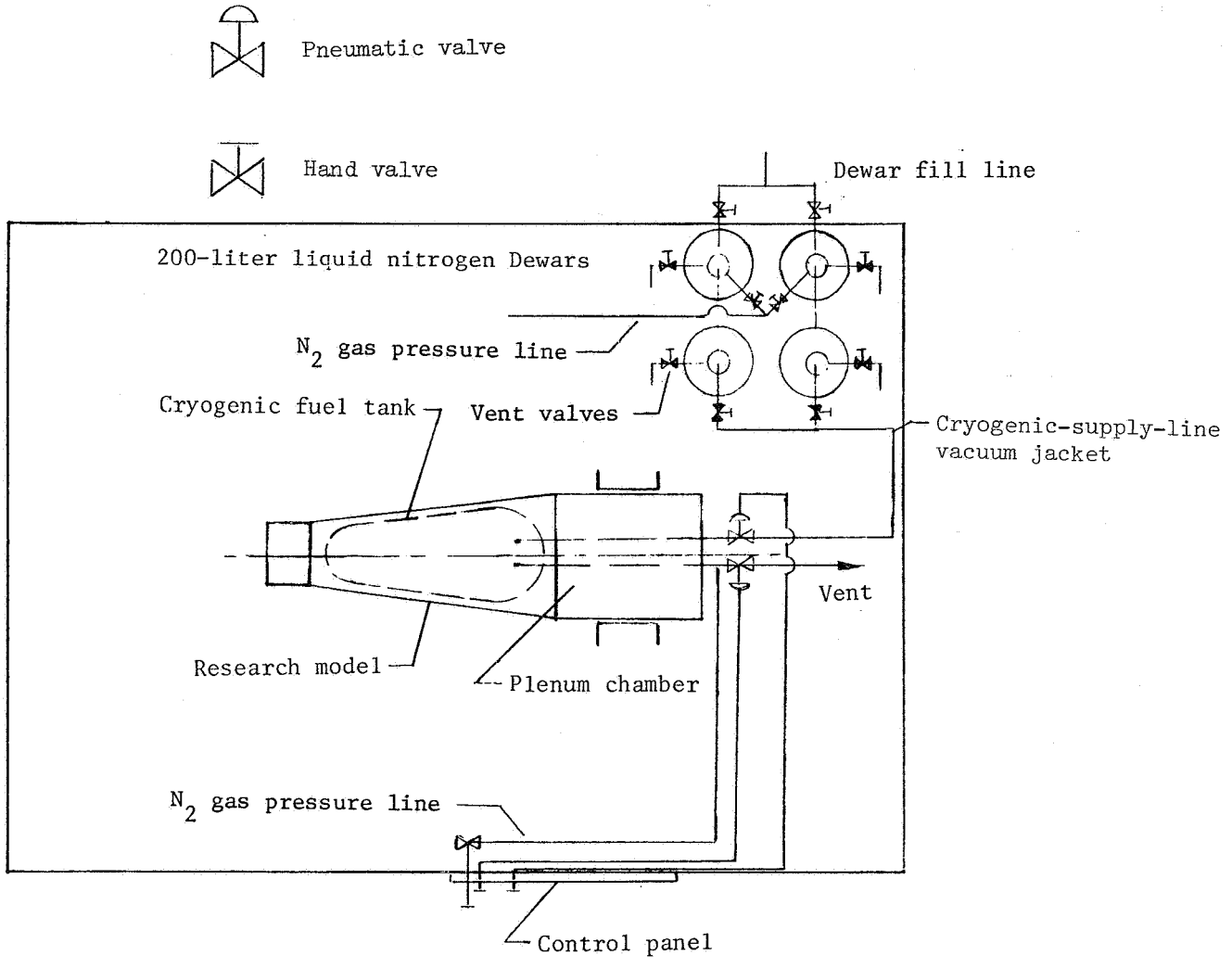

Figure 7.- Cryogenic storage and transfer system.

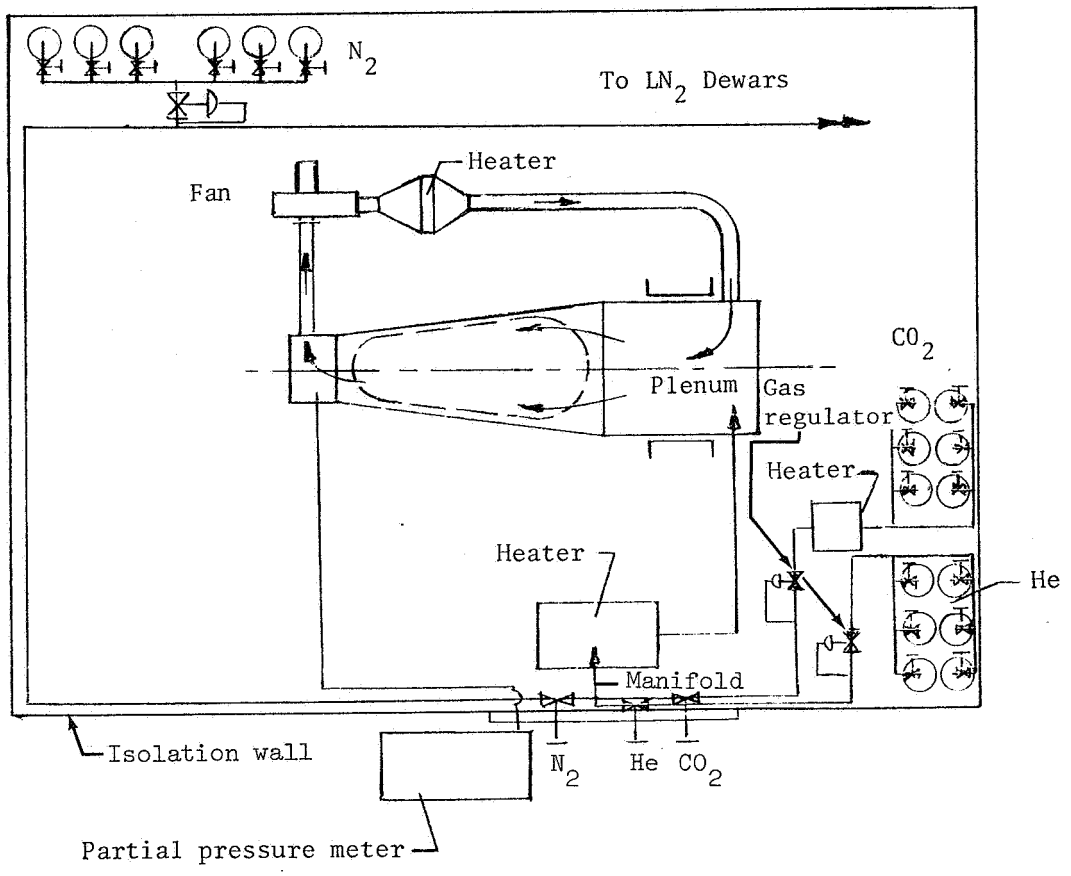

Figure 8.- Purge gas system.

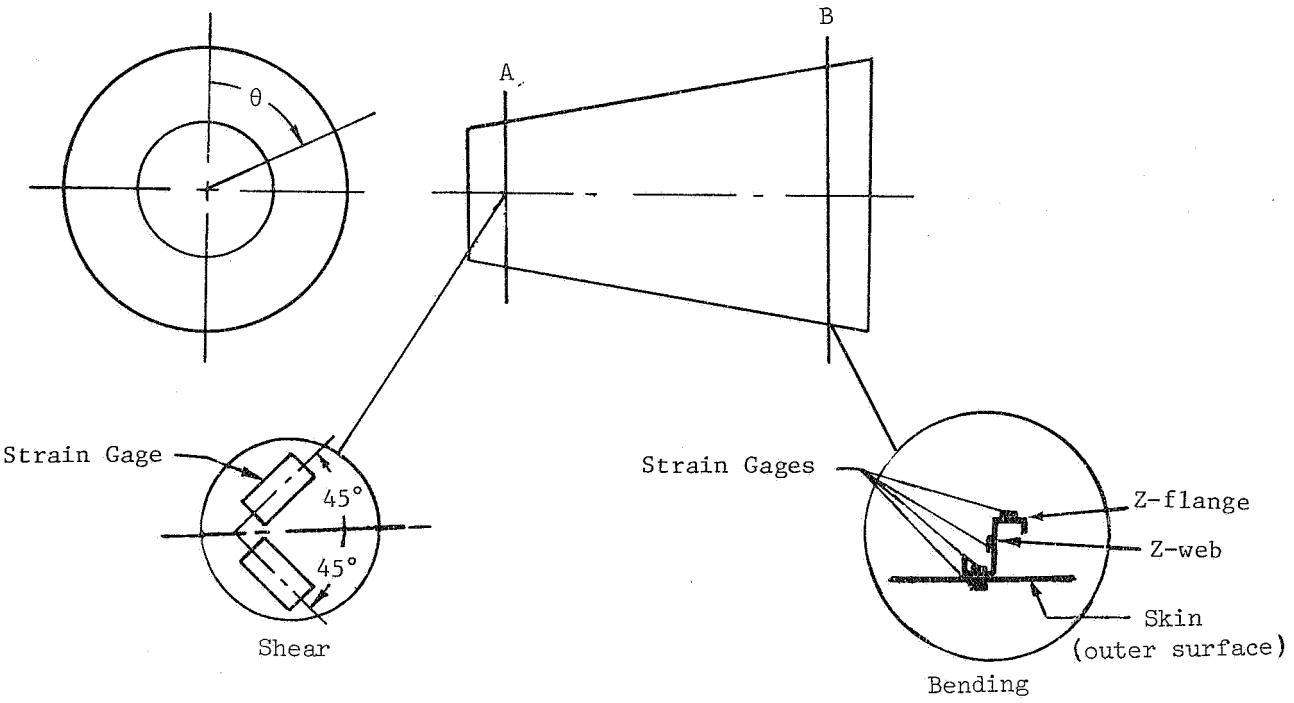

Strain gage	Station (a)	θ, deg	Type	Location
1	A	0	Bending	Z-flange
2	A	0	Bending	Z-web
3	A	180	Bending	Z-flange
4	A	180	Bending	Z-web
5 and 6	A	270	Shear	Skin (inner)
7 and 8	A	90	Shear	Skin (inner)
9	A	315	Bending	Skin (inner)
10	A	45	Bending	Skin (inner)
11	B	0	Bending	Z-flange
12	B	0	Bending	Z-web
13	B	180	Bending	Z-flange
14	B	180	Bending	Z-web
15 and 16	B	90	Shear	Skin (inner)
19	B	45	Bending	Skin (inner)
20	B	315	Bending	Skin (inner)
21	A	0	Bending	Skin (outer)
22	A	180	Bending	Skin (outer)
23 and 24	A	270	Shear	Skin (outer)
28	A	45	Bending	Skin (outer)
29	B	0	Bending	Skin (outer)
30	B	180	Bending	Skin (outer)
31 and 32	B	90	Shear	Skin (outer)
35	B	45	Bending	Skin (outer)
36	B	315	Bending	Skin (outer)

[a] Station A is 22.2 cm (8.75 in.) from the small end and station B is 9.4 cm (3.7 in.) from the large end.

Figure 9.- Strain-gage locations.

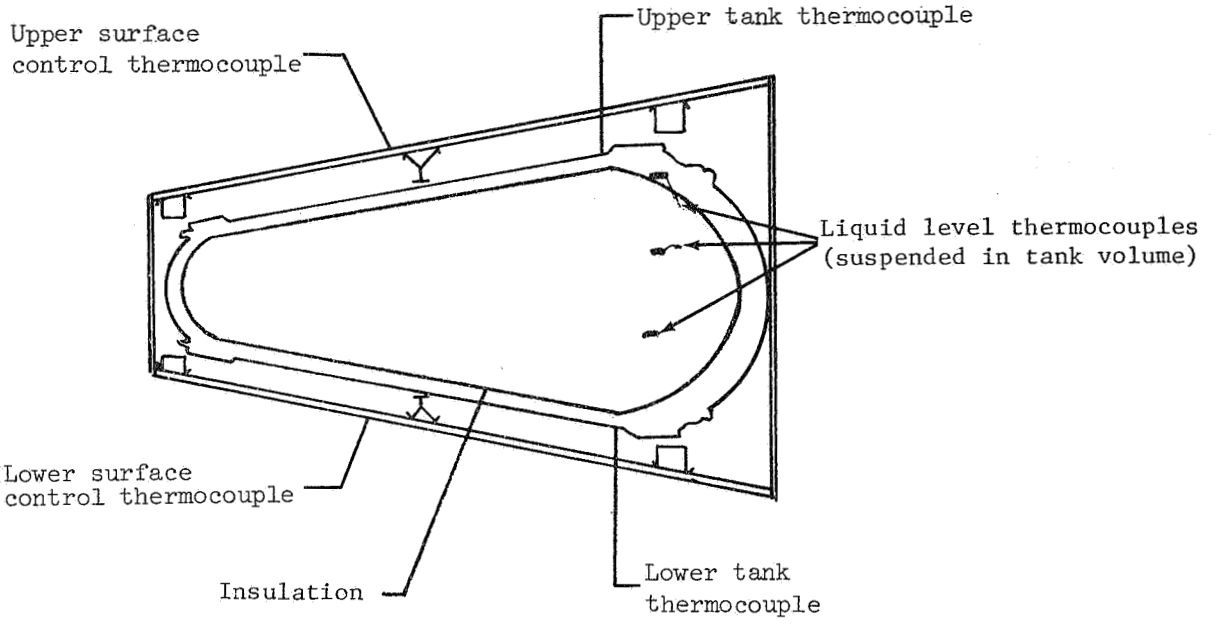

Figure 10.- Thermocouple locations in test model.

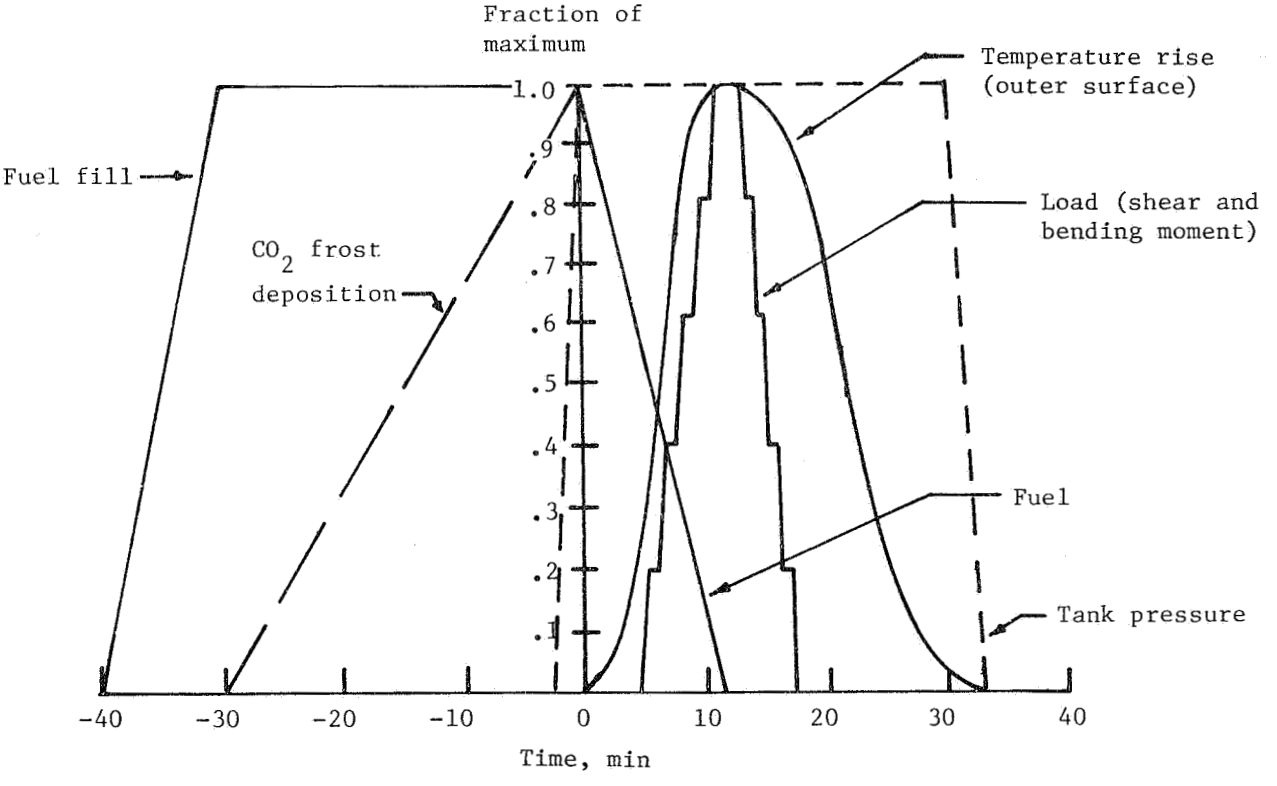

Figure 11.- Simulated hypersonic flight test conditions.

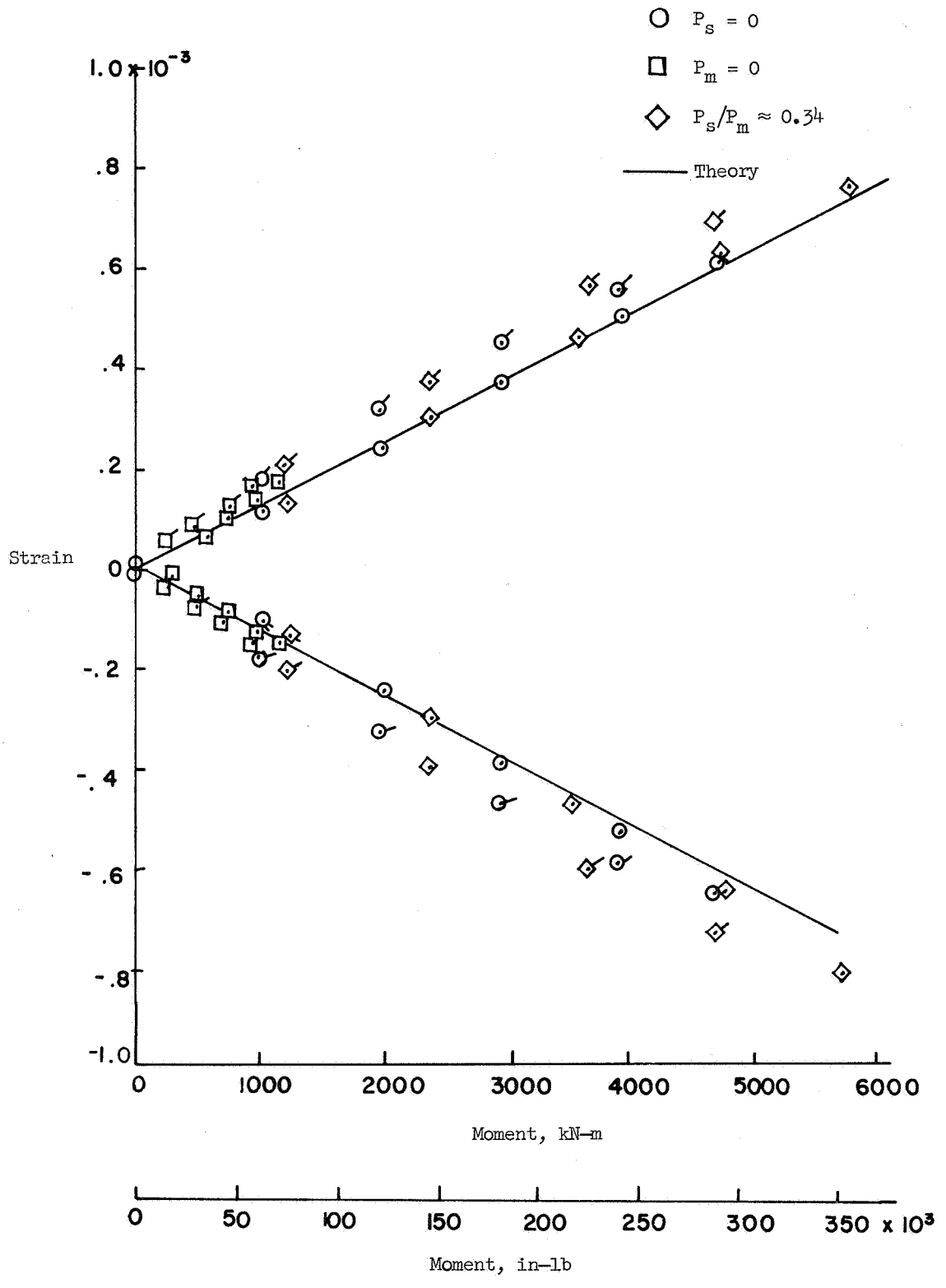

(a) Upper and lower surfaces.

Figure 12.- Measured strains at forward station for three loading conditions. (Flagged symbols denote unloading.)

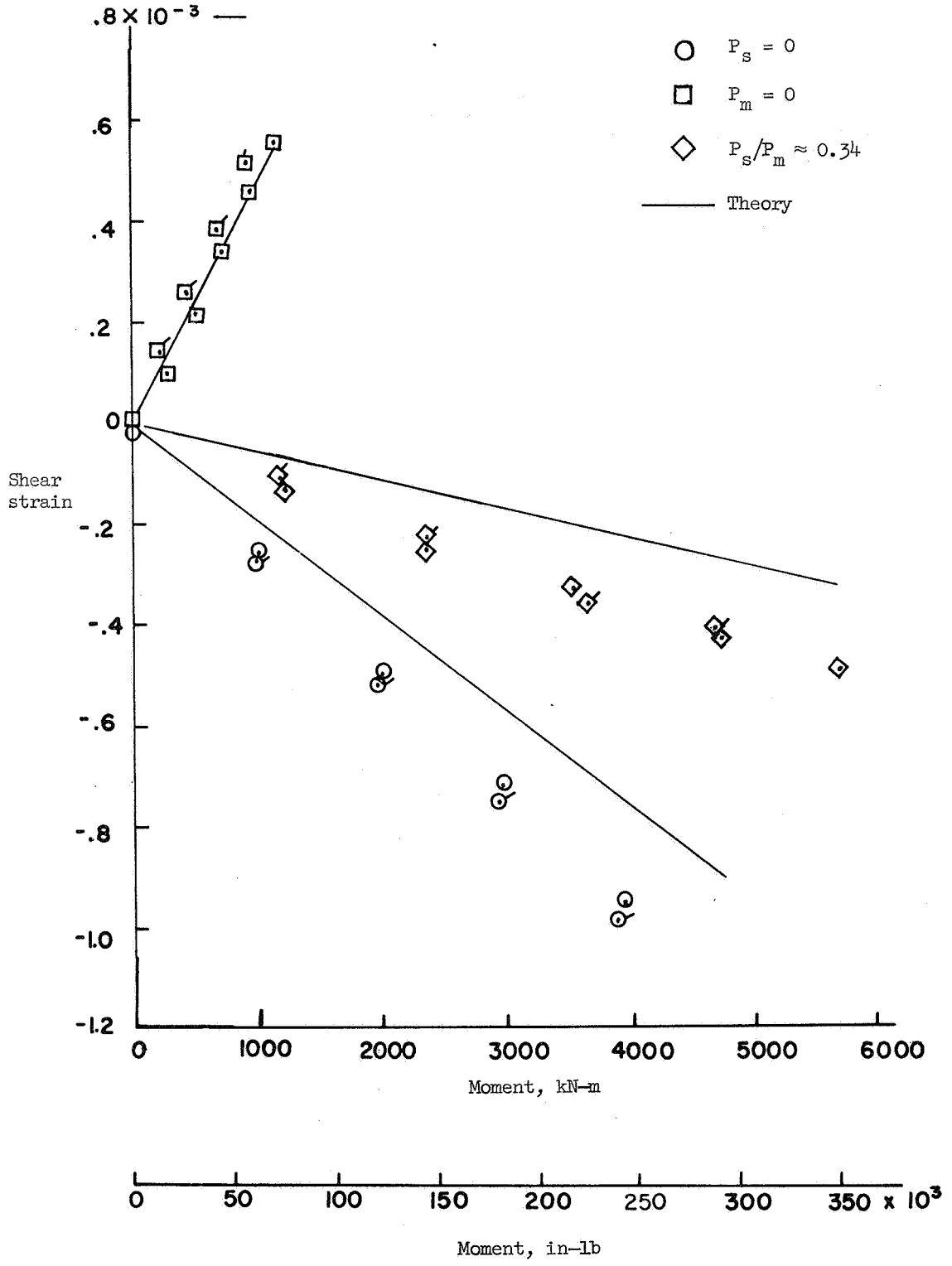

(b) Side surface (shear).

Figure 12.- Concluded.

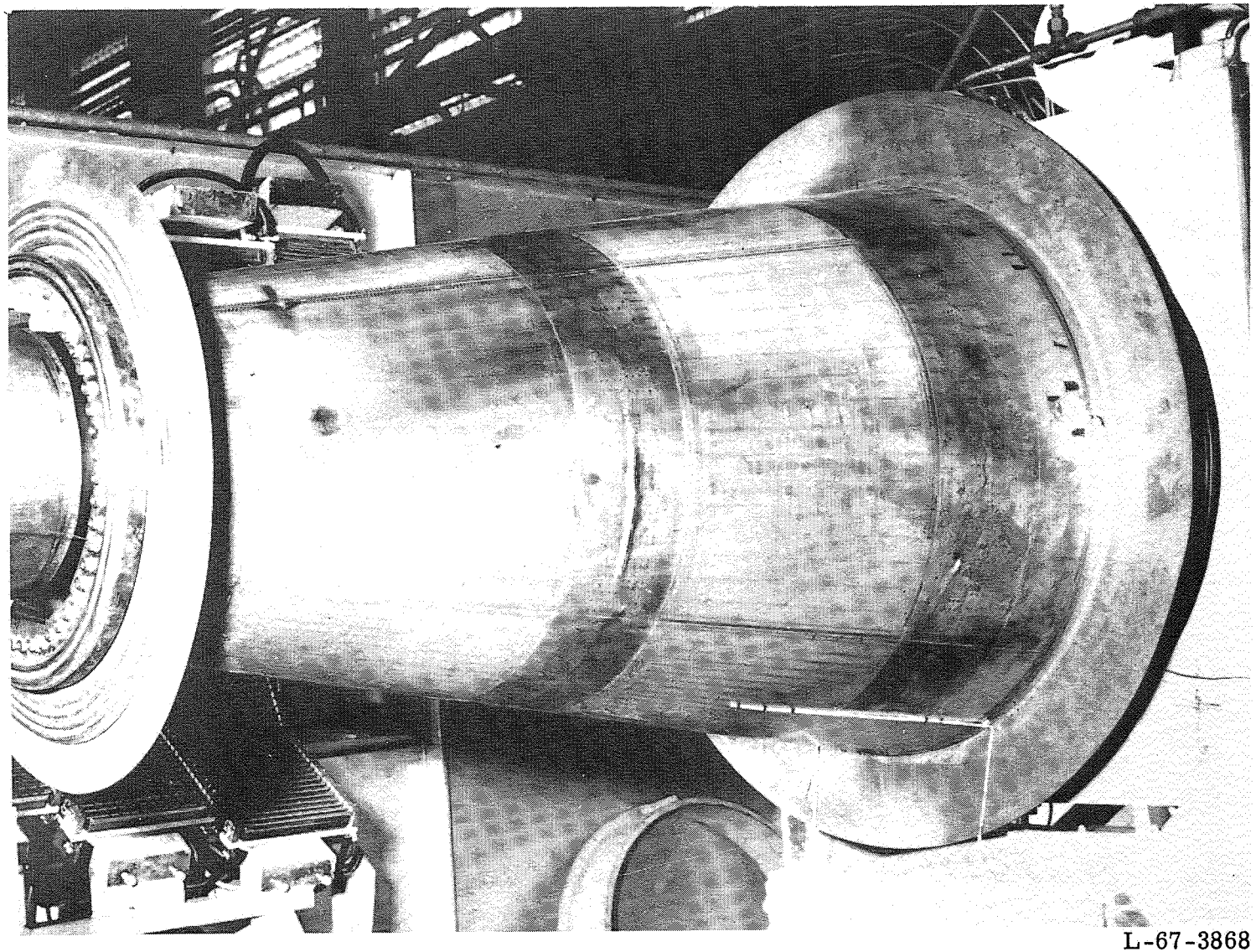

L-67-3868

(a) After first test.

Figure 13.- Circumferential joint buckles.

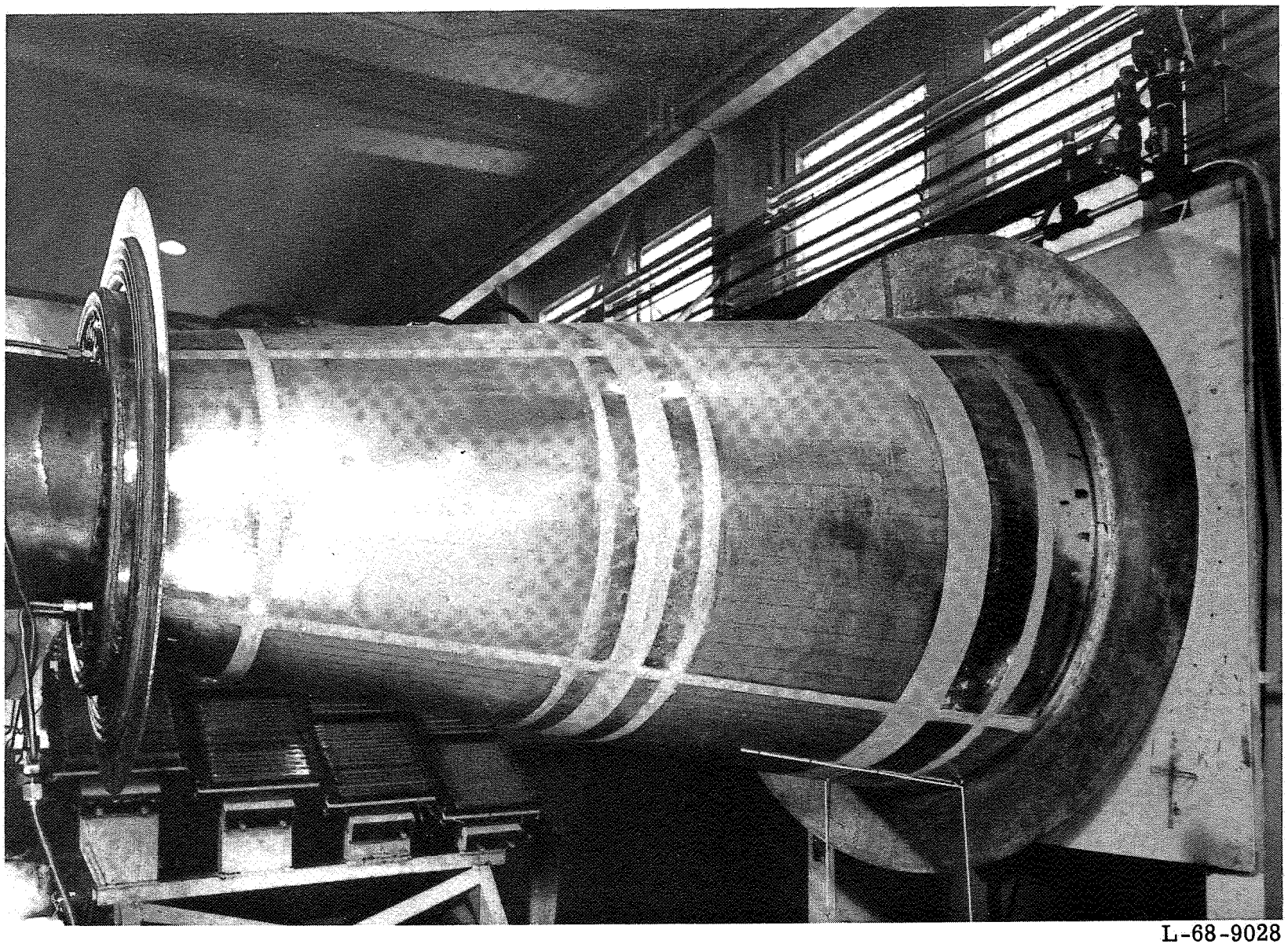

L-68-9028

(b) After second test.

Figure 13.- Concluded.

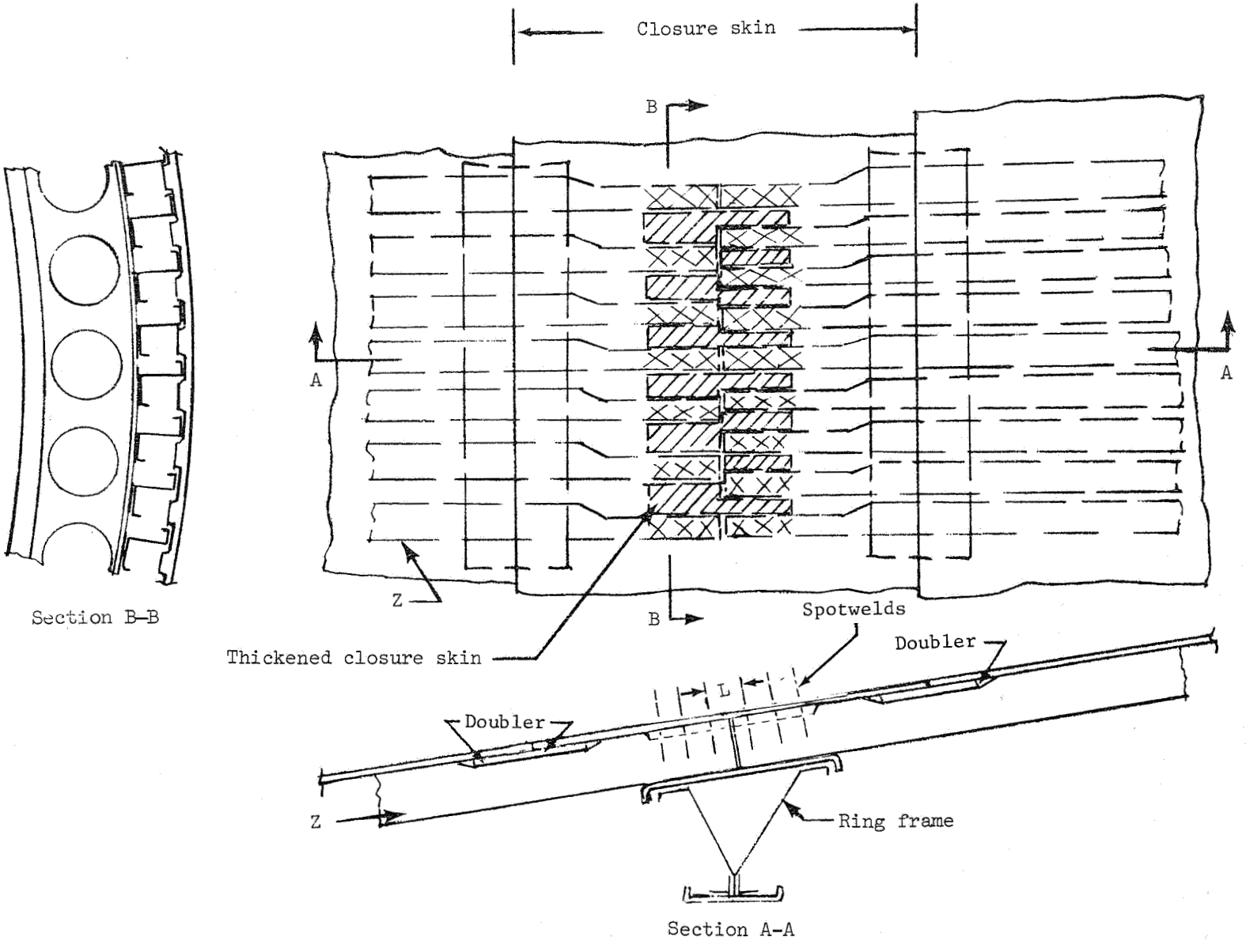

Figure 14.- A typical joint between panels.

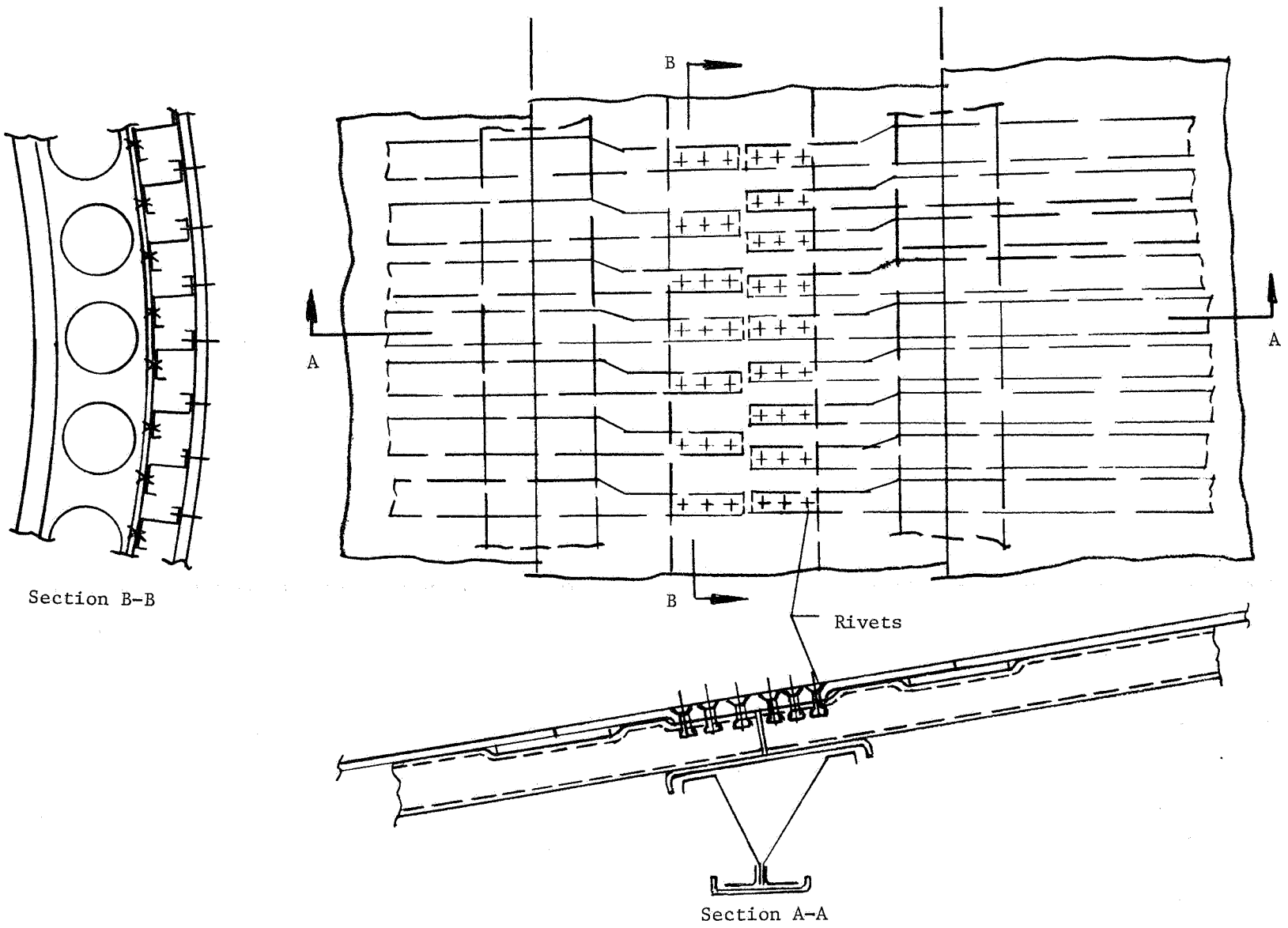

Figure 15.- Improved structural joint design.

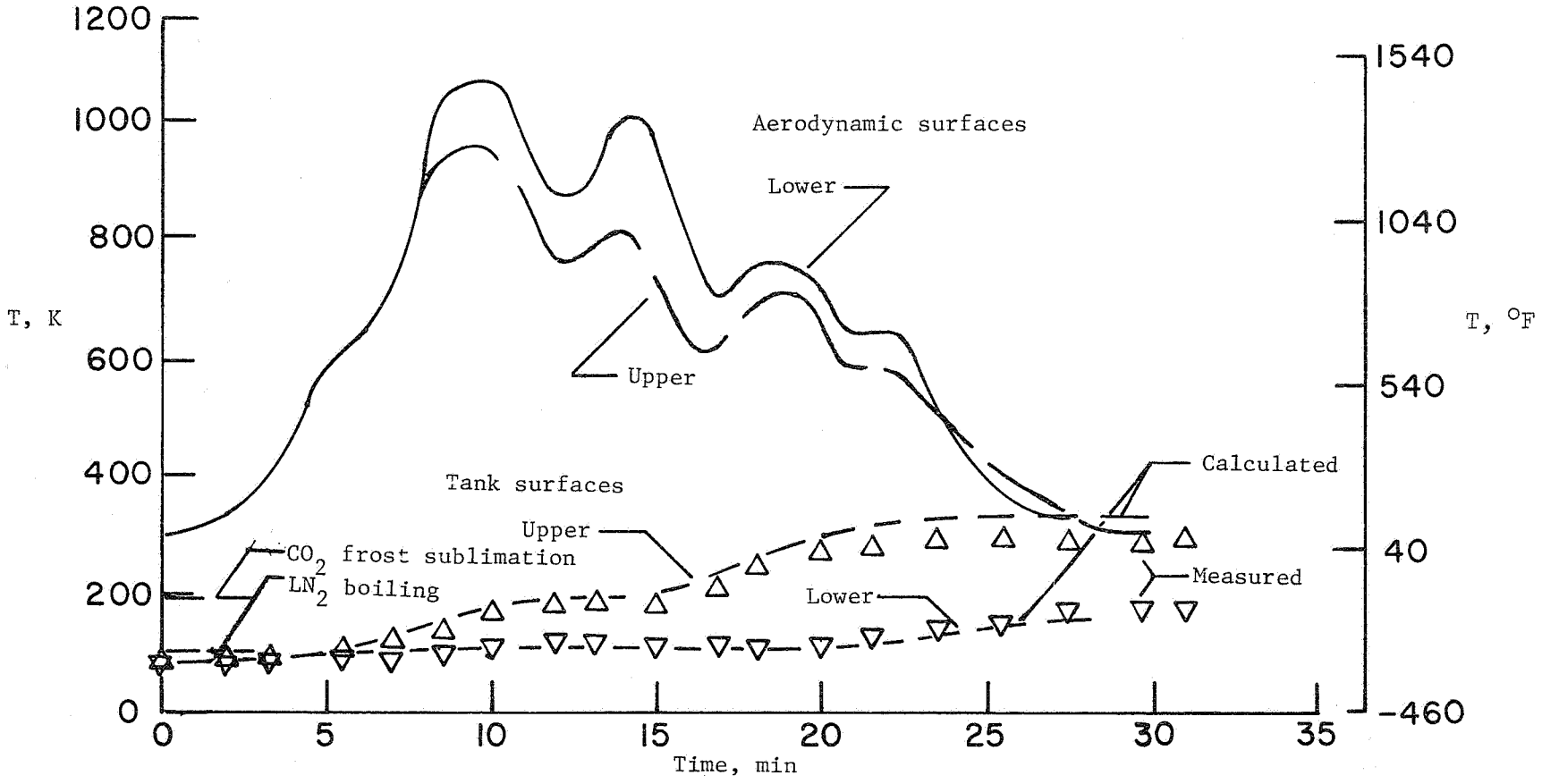

(a) Test 1.

Figure 16.- Temperature histories of simulated flight tests.

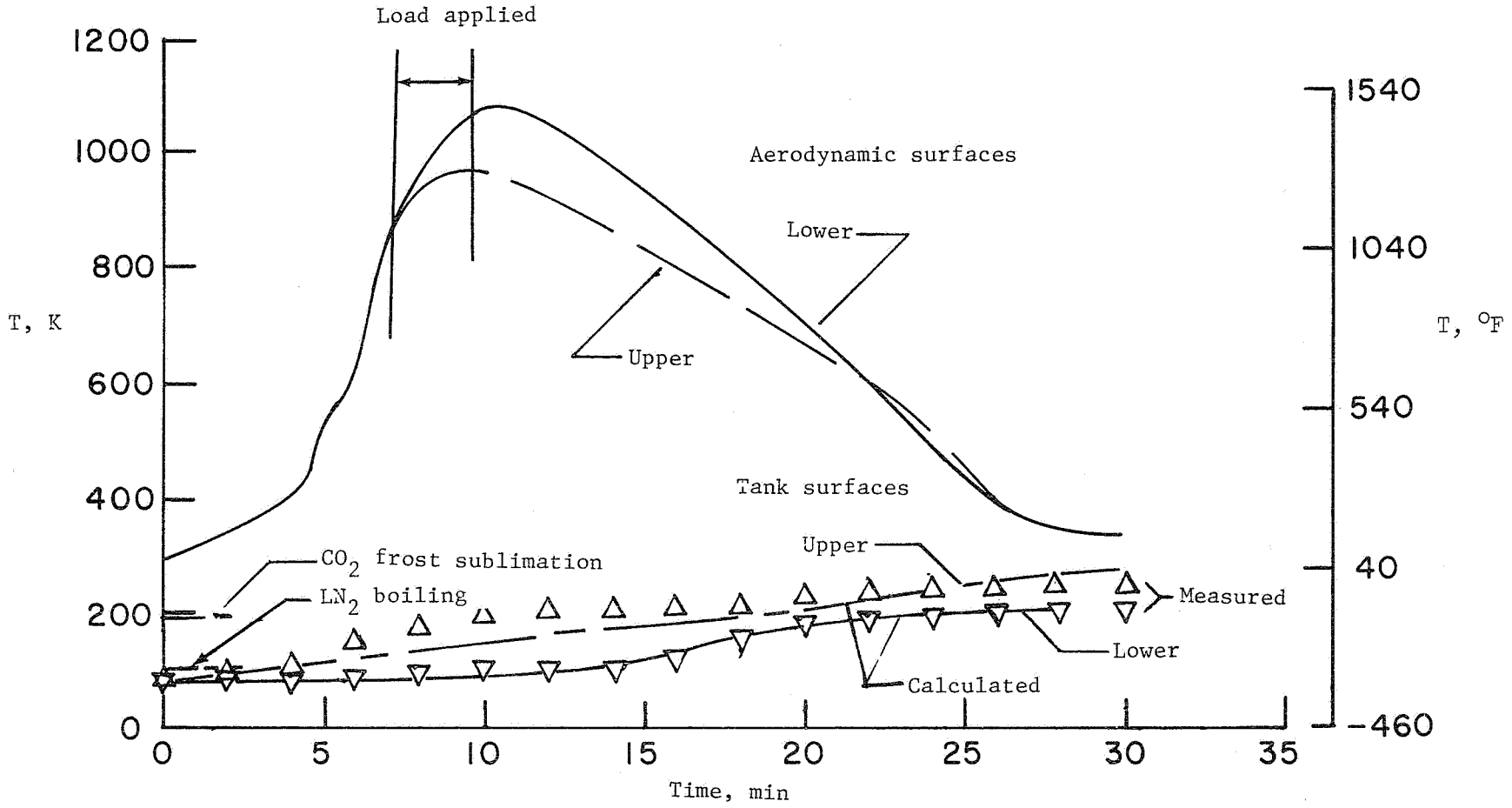

(b) Test 3.

Figure 16.- Concluded.

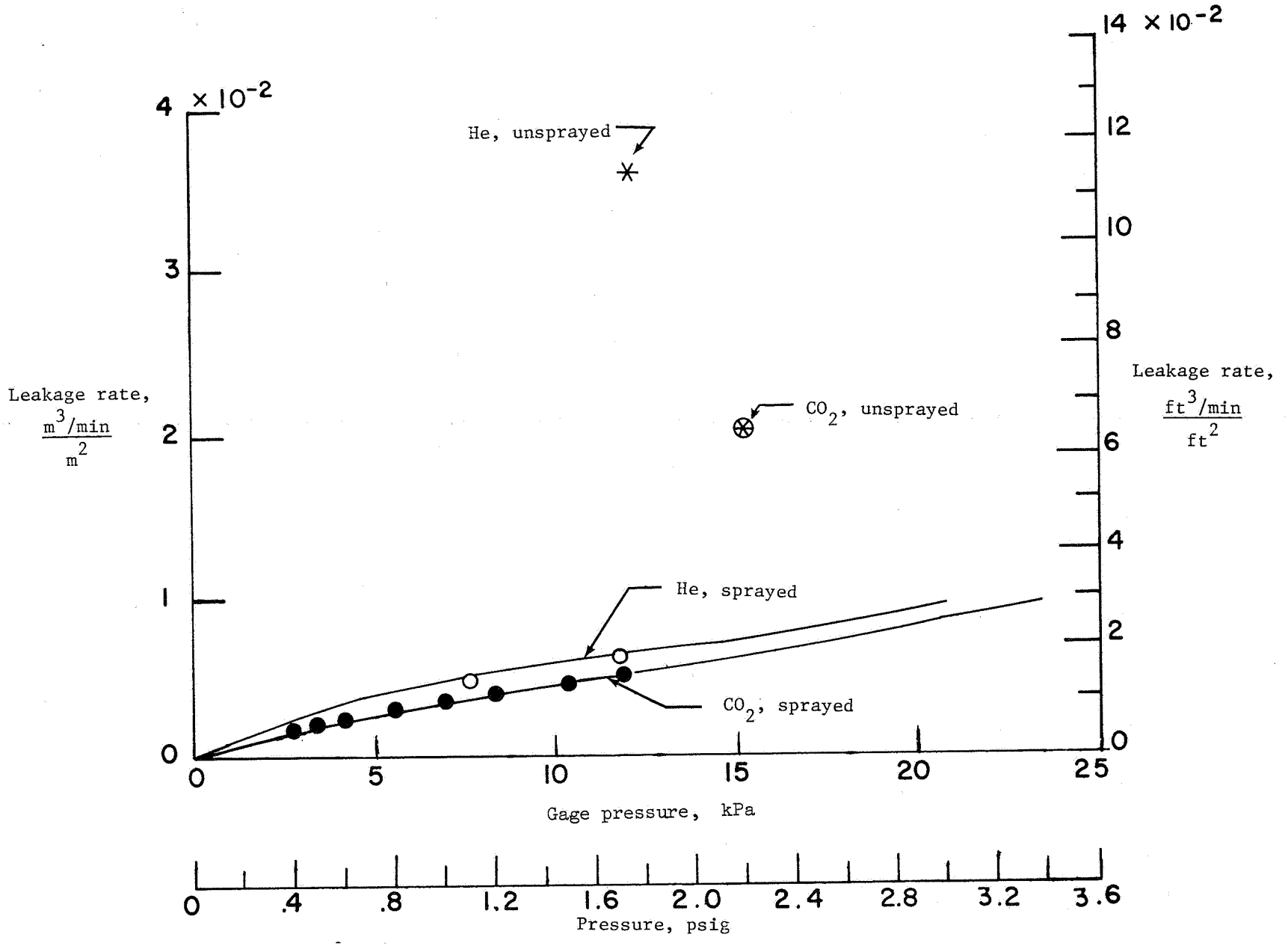

Figure 17.- Purge gas leakage rates with and without flame-sprayed joints.

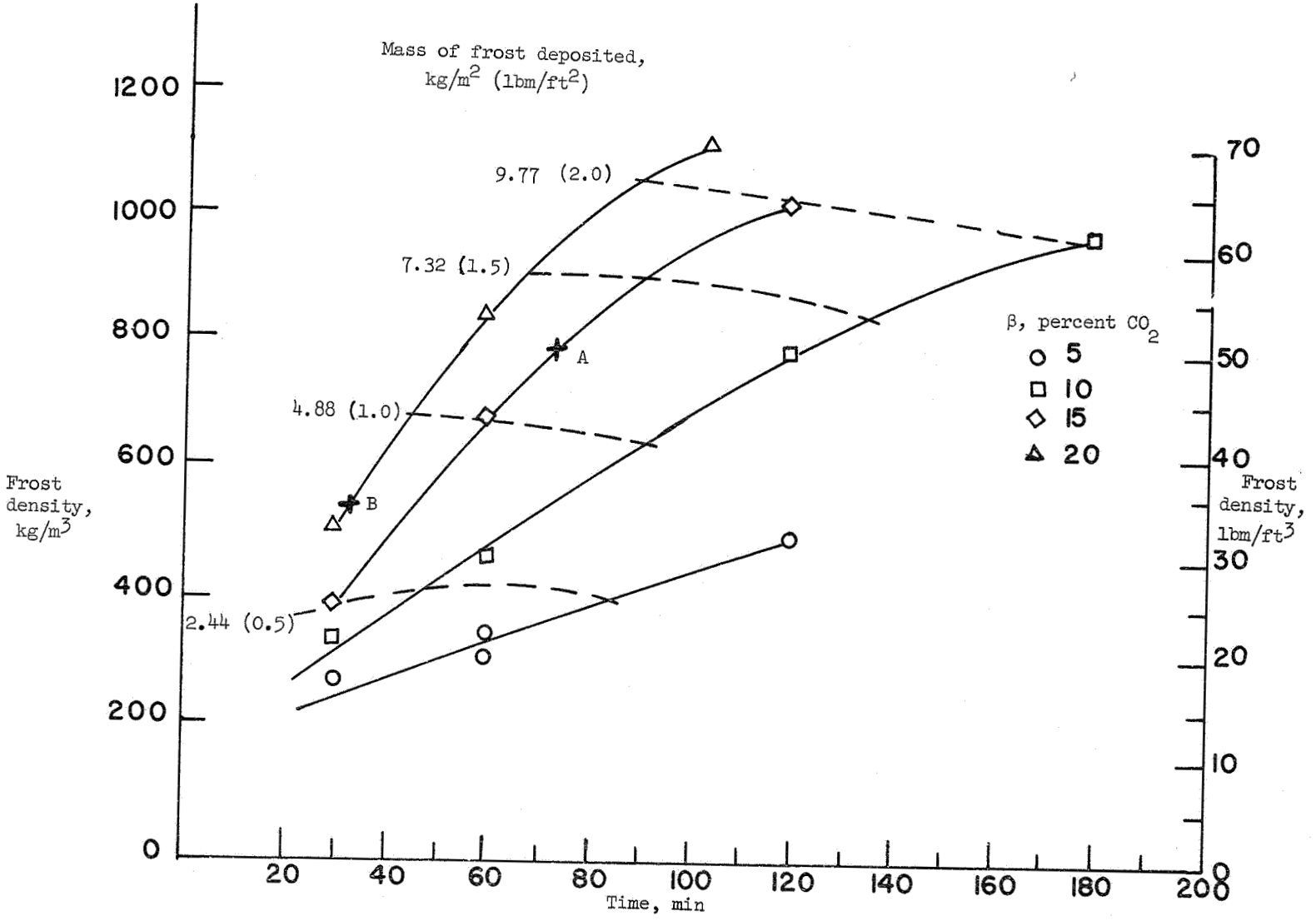

Figure 18.- Carbon dioxide cryodeposition test results using 0.89 cm (0.35 in.) of fibrous insulation. (A and B denote conditions for tests 1 and 3, respectively.)

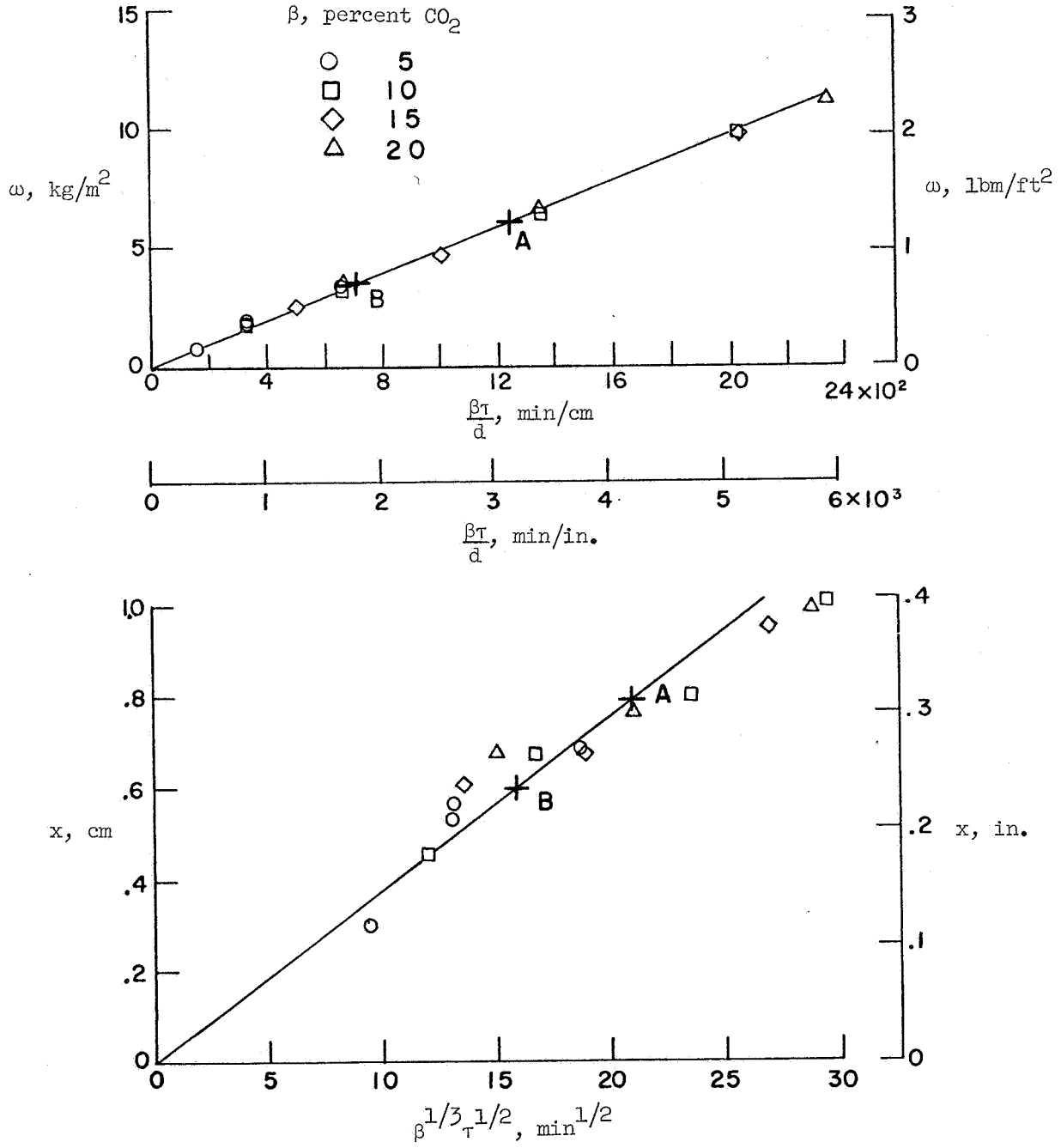

Figure 19.- Deposition results correlated with the parameters of reference 10. (A and B denote conditions for tests 1 and 3, respectively.)